

Measuring black hole masses from tidal disruption events and testing the $M_{\text{BH}} - \sigma_*$ relationZ.Q. ZHOU,¹ F.K. LIU*,^{1,2} S. KOMOSSA,³ R. CAO,¹ L.C. HO,^{2,1} XIAN CHEN,^{1,2} AND SHUO LI^{4,1}¹*Department of Astronomy, School of Physics, Peking University, Beijing 100871, China*²*Kavli Institute for Astronomy and Astrophysics, Peking University, Beijing 100871, China*³*Max Planck Institut für Radioastronomie, Auf dem Hügel 69, 53121 Bonn, Germany*⁴*National Astronomical Observatories, Chinese Academy of Sciences, Beijing 100012, China*

ABSTRACT

Liu and colleagues recently proposed an elliptical accretion disk model for tidal disruption events (TDEs). They showed that the accretion disks of optical/UV TDEs are large and highly eccentric and suggested that the broad optical emission lines with complex and diverse profiles originate in the cool eccentric accretion disk of random inclination and orientation. In this paper, we calculate the radiation efficiency of the elliptical accretion disk and investigate the implications for the observations of TDEs. We compile the observational data of the peak bolometric luminosity and the total radiation energy after peak brightness of 18 TDE sources and compare the observations to the expectations from the elliptical accretion disk model. Our results show that the observations are well consistent with the expectations and that the majority of the orbital energy of the stellar debris is advected onto the black hole (BH) without being converted into radiation. By comparing the observations and the expectations, we derive the masses of the disrupted stars and BHs of the TDEs. The BH masses obtained in this paper are well consistent with those calculated with the $M_{\text{BH}} - \sigma_*$ relation. Our results provide an effective method to measure the masses of BHs from thousands or more of the TDEs to be discovered in the ongoing and next-generation sky surveys, no matter whether the BHs are located at the centers of the galactic nuclei or wandering in disks and halos.

Keywords: accretion, accretion disk — black hole physics — galaxies: active — quasars: supermassive black holes — stars: black holes

1. INTRODUCTION

A star may be tidally destroyed (Hills 1975; Rees 1988; Evans & Kochanek 1989; Lodato et al. 2009; Hayasaki et al. 2013; Shiokawa et al. 2015; Bonnerot et al. 2016; Sądowski et al. 2016), when it is scattered closely flying by a supermassive black hole (SMBH) (Magorrian & Tremaine 1999; Wang & Merritt 2004; Chen et al. 2008, 2009; Liu et al. 2009; Liu & Chen 2013; Li et al. 2017). At tidal disruption, about half of the stellar debris loses orbital energy and becomes bound to the BH. The bound stellar debris returns to the orbital pericenter of the star and circularizes to form accretion onto the BH. In the canonical model for tidal disruption event (TDE), the material streams are assumed to be circularized rapidly due to strong

relativistic apsidal precession and the accretion disk has a size of about twice the orbital pericenter of the star (Rees 1988). In this scenario, the accretion disk of TDEs is an outer-truncated analogue of the accretion disk of active galactic nuclei (AGNs) and galactic X-ray binaries and radiates mainly in soft X-rays. The radiation in optical/UV wavebands are expected to be rather weak and decay with time in a power law much shallower than the fallback rate of the stellar debris (Strubbe & Quataert 2009). No strong broad optical emission line is expected with the hot accretion disk.

The observations of non-jetted TDEs discovered in the X-rays are broadly consistent with the expectations, but those discovered in the optical/UV wavebands challenge the canonical model (Komossa & Bade 1999; Gezari et al. 2006; van Velzen et al. 2011; Liu et al. 2014; Komossa 2015, for a recent review). Most TDEs and candidates discovered in the optical/UV wavebands emit radiation mainly in optical/UV wavebands and little or no radiation in soft X-rays (e.g. Komossa et al. 2008; Wang et al. 2012; Gezari et al. 2012; Holoien et al. 2014, 2016a; Blagorodnova et al. 2019; Leloudas et al. 2019). The optical/UV luminosities unexpectedly follow the fallback rate of the stellar debris (Gezari et al. 2012; Arcavi et al. 2014; Hung et al. 2017; Wevers et al. 2017; Mockler et al. 2019) and the observed radiated energy or the observed accreted material onto the BH and the implied mass of the disrupted star can be up to orders of magnitude smaller than the expectations of the tidal disruptions of main-sequence stars or brown dwarfs (Li et al. 2002; Komossa et al. 2004; Halpern et al. 2004; Esquej et al. 2008; Gezari et al. 2008, 2009, 2012; Cappelluti et al. 2009; Maksym et al. 2010; Chornock et al. 2014; Donato et al. 2014; Holoien et al. 2014, 2016a,b; Liu et al. 2014; Blagorodnova et al. 2017; Hung et al. 2017; Mockler et al. 2019; Saxton et al. 2017, 2018). Most optical/UV TDEs and candidates have strong broad optical emission lines with complex, asymmetric, and diverse profiles (Komossa et al. 2008; Wang et al. 2012; Gezari et al. 2012; Arcavi et al. 2014; Holoien et al. 2014, 2016a,b, 2019a).

It was recently suggested in the literature that strong winds form during the super-Eddington accretion and the soft X-ray radiation emitted by the accretion disk are absorbed and reprocessed into UV wavebands by the optically-thick wind envelopes (e.g. Dai et al. 2018). The broad optical emission lines are powered by the soft X-ray and forming in the surface layers of the optically thick envelopes (Roth et al. 2016). However, the strong outflow may make the observed light curve to significantly diverge from the fallback rate of stellar debris (Strubbe & Quataert 2009; Lodato & Rossi 2011). The analytic and hydrodynamic simulations of stellar tidal disruptions (Rees 1988; Evans & Kochanek 1989; Kochanek 1994; Hayasaki et al. 2013; Guillochon et al. 2014; Dai et al. 2015; Piran et al. 2015; Shiokawa et al. 2015; Bonnerot et al. 2016; Hayasaki & Loeb 2016; Sądowski et al. 2016) indicate that the bound stellar streams circularize due to the self-interaction of the streams returning at different time because of general relativistic apsidal precession and the rapid formation of accretion disk happens only in tidal disruptions of stars with orbital pericenter about the innermost stable circular orbit (ISCO) of Schwarzschild BH (Shiokawa et al. 2015; Bonnerot et al. 2016; Hayasaki & Loeb 2016; Dai et al. 2015).

The tidal disruption radius of solar-type star by BH of mass $\lesssim 10^{6.5} M_{\odot}$ with M_{\odot} the solar mass is much larger than the ISCO and the general relativistic apsidal precession of bound streams of most TDEs is expected to be inefficient in circularizing the streams (Shiokawa et al. 2015). Because the collision of the streams due to the general relativistic apsidal precession occurs at nearly the apocenter of the most bound stellar debris, the liberated kinetic energy by the collision shocks are roughly comparable to the observations of the optical/UV TDEs. In the literature, the optical/UV TDEs are suggested to be powered by the energy liberated during the formation of the accretion disk rather than during the subsequent accretion of matter onto the BH (Piran et al. 2015). Although the observed luminosities, temperature and emission radii can

roughly be explained with the model of collision shocks, the energy dissipated by the collision shocks is only about 1% of the total energy available from accretion onto the black hole. As noted by the original work (Piran et al. 2015), the problem with the collision-shock model is: why do we see only 1% of the expected energy and miss the majority of the energy? It is argued that the emissions during the formation of accretion disk may dominate the radiation of TDEs if the eccentricity of accretion disk is excited during the subsequent accretion of matter so significantly that the orbital pericenter of the fluid elements decreases to the marginal stable orbit of black hole with little decrease of the semimajor axis of fluid elements (Svirski et al. 2017).

It is generally believed in the literature that double-peaked broad Balmer emission lines of AGNs originate in accretion disk (Chen & Halpern 1989; Chen et al. 1989; Storchi-Bergmann et al. 1993, 2017; Eracleous & Halpern 1994, 2003; Strateva et al. 2003; Popović et al. 2004). By modeling the double-peaked H α emission line of the optical/UV TDE PTF09djl, Liu et al. (2017) showed that the accretion disk of TDEs is large and extremely eccentric of eccentricity without significant variation from the outer to inner edges of elliptical accretion disk. The extreme eccentricity is determined jointly by the elliptical orbit of the most bound stellar debris and the self-interaction of streams. Liu and colleagues showed that the diversities and time variations of the observed profiles of the broad optical emission lines of the optical/UV TDE ASASSN-14li are mainly due to the differences of the inclination and orientation of elliptical accretion disk and the disk precession due to Lens-Thirring effect (Cao et al. 2018). The emissions of the accretion disk of constant eccentricity would dominate the radiation of TDEs and the emissions during the formations of accretion disk are negligible. The three-dimensional radiative hydrodynamic simulations of stream collisions show that the majority of the kinetic energy dissipated by the collision shock is converted back to the kinetic energy of the downstream gas and only about 2%-8% of the energy can be radiated away during the formation of accretion disk (Jiang et al. 2016), leading to the conclusion of disk emissions dominating the radiation of TDEs even more certain. The elliptical accretion disks of large semimajor axis and extreme eccentricity give low conversion factors of matter into radiation of PTF09djl (Liu et al. 2017) and ASASSN-14li (Cao et al. 2018), which are, respectively, consistent with the radiation efficiencies obtained from the analysis of the light curves of PTF09djl and ASASSN-14li (Mockler et al. 2019). The expected peak energy luminosities from the accretion onto the black hole are well consistent with the observations of PTF09djl and ASASSN-14li (Liu et al. 2017; Cao et al. 2018).

Here we adopt the relativistic elliptical accretion disk model for TDEs given in Liu et al. (2017). We assume that the unbound outflows from the collision shocks during the formation of accretion disk (Jiang et al. 2016) and from the surface of the cool elliptical accretion disk, if any, are only a small fraction of the fallback stellar debris. Because we are interested in only the total radiation efficiency of the accretion onto black holes, we do not distinguish the emissions of radiation from the collision shocks during the formation of accretion disk and from the subsequent accretion of elliptical accretion disk. With the elliptical accretion disk, we calculate the conversion efficiency of matter into radiation of TDEs during the accretion of matter onto black holes, which in the literature is always assumed to be a free parameter in modeling the luminosities of TDEs (e.g. Liu et al. 2014; Mockler et al. 2019). With the radiation efficiency, we can calculate the expected peak luminosity and total radiation energy of TDEs and compare the expectations with the observations of non-jetted TDEs in the literature. We will show that the peak luminosity and the total radiation energy expected with the elliptical accretion disk are well consistent with the observations of the non-jetted TDEs and candidates. In the elliptical accretion disk model for Schwarzschild black hole, the radiation efficiency is not a constant but depends significantly on the masses of BH and star. With the

observations of the peak luminosity and the total radiation energy of non-jetted TDEs, we can derive the masses of black holes and stars. This is the first method to uniquely measure the mass of stars at distant galaxies. Because the masses of BHs at galactic nuclei can be calculated with the well-known correlations of the BH mass and the bulge properties of host galaxies, we will show that the BH masses obtained in this paper are well consistent with those calculated with the correlation of BH mass and the stellar velocity dispersion of host galaxies. The work in this paper provide an accurate technique to weigh both the BHs and stars no matter whether they hide in deep center of galactic nuclei and globular cluster or wonder around the galactic disk.

The paper is organized as follow. In section 2, we present the elliptical disk model for TDEs and calculate the radiation efficiency. Section 3 gives the peak luminosity and the total radiation energy after peak expected with the elliptical accretion disk model. In section 4, we compile the observational data of the peak bolometric luminosity and the total radiation energy after peak brightness of 18 non-jetted TDE sources and compare the observations and the expectations of the disk model. We calculate the masses of BHs and stars with the observations of the peak luminosity and the total radiation energy after peak and compare the results with those obtained with the correlation of BH mass and bulge properties of host galaxies in section 5. The discussions and conclusions are given in section 6.

2. ELLIPTICAL ACCRETION DISK AND RADIATION EFFICIENCY OF TDES

We begin the calculation of radiation efficiency by introducing the formation of the elliptical accretion disk of TDEs. A star is tidally destroyed when it passes by a SMBH with orbital pericenter r_p smaller than the tidal disruption radius

$$r_t = R_* (M_{\text{BH}}/M_*)^{1/3} \simeq 23.557 r_* m_*^{-1/3} M_6^{-2/3} r_s, \quad (1)$$

where $M_{\text{BH}} = 10^6 M_6 M_\odot$ is the mass of the BH, r_s is the BH Schwarzschild radius, and $R_* = r_* R_\odot$ and $M_* = m_* M_\odot$ are, respectively, the stellar radius and mass. In this paper, if needed, we calculate the radius with the mass-radius relation $R_* \simeq R_\odot (M_*/M_\odot)^{1-\zeta}$ of main sequence stars and $\zeta \simeq 0.21$ and $\zeta \simeq 0.44$ are, respectively, for stellar masses $0.1 M_\odot < M_* \leq 1 M_\odot$ and $1 M_\odot < M_* < 150 M_\odot$ (Kippenhahn et al. 2012). In the literature, hydrodynamic simulations of tidal disruptions have been done mainly with main sequences. Here we extrapolate the results of main sequence stars with the same polytropic index to brown dwarfs (BDs) but notice that the results with BDs have larger uncertainties. For BDs of masses $0.01 M_\odot < M_* \leq 0.07 M_\odot$, we use the mass-radius relation of BDs of age $t = 5$ Gyr, $R_* \simeq 0.06 R_\odot (M_*/M_\odot)^{1-\zeta}$ with $\zeta = 9/8$ (Chabrier & Baraffe 2000). For stars with mass $0.07 M_\odot < M_* < 0.08 M_\odot$, we adopt a bridge relation $R_* = 0.136 R_\odot (M_*/0.08 M_\odot)^{1-\zeta}$ with $\zeta = -2.637$.

After tidal disruption, the bound stellar debris returns to the pericenter of the star and forms accretion disk mainly due to the shocks of the interaction between the post-pericenter outflowing and freshly inflowing streams because of relativistic apsidal precession (Evans & Kochanek 1989; Kochanek 1994; Hayasaki et al. 2013; Dai et al. 2015; Shiokawa et al. 2015; Bonnerot et al. 2016; Hayasaki & Loeb 2016). The location and conservation of angular momentum of stream collisions together give the semimajor axis of the disk

$$a_d \simeq \frac{2r_p}{2\delta + \sin^2(\Omega/2)} \simeq \frac{2\beta^{-1}r_t}{2\delta + \sin^2(\Omega/2)} \quad (2)$$

and the eccentricity

$$e_d \simeq \left[1 - \frac{(1 - e_{\text{mb}}^2) a_{\text{mb}}}{a_d} \right]^{1/2} \simeq \left[1 - 2\delta - \sin^2 \left(\frac{\Omega}{2} \right) \right]^{1/2} \simeq [1 - 2\delta(1 + \Delta)]^{1/2} \quad (3)$$

with $\Delta = \sin^2(\Omega/2)/(2\delta)$ (Liu et al. 2017; Cao et al. 2018), where $\beta = r_t/r_p$ is the orbit penetration factor of star, $a_{\text{mb}} \simeq r_t^2/2R_*$ nearly independent of the penetration factor β (Guillochon & Ramirez-Ruiz 2013; Hayasaki et al. 2013) and $e_{\text{mb}} = 1 - \delta$ with $\delta \simeq 2R_*r_p/r_t^2 \simeq 0.02\beta^{-1}m_*^{1/3}M_6^{-1/3}$ are, respectively, the orbital semimajor axis and eccentricity of the most bound stellar debris. In equations (2) and (3), Ω is the instantaneous de Sitter precession at periapse of the most-bound stellar debris

$$\Omega \simeq \frac{6\pi GM_{\text{BH}}}{c^2(1-e_{\text{mb}}^2)a_{\text{mb}}} \simeq \frac{3\pi r_s}{(1+e_{\text{mb}})r_p} \simeq \frac{3\pi}{2-\delta}\beta\frac{r_s}{r_t}. \quad (4)$$

For tidal disruption of star with orbital pericenter $r_p < 10r_s$, we have $\Delta \gtrsim 1$ and the relativistic apsidal precession of the bound stellar debris becomes important and significantly reduces the eccentricity of the accretion disk.

The modeling of the double-peaked and/or asymmetric broad optical emission lines of TDEs shows that the eccentricity remains nearly unchanged over disk (Liu et al. 2017; Cao et al. 2018), which suggest a rapid accretion of matter onto BH and a slow circularization of stellar streams. A rapid accretion of matter onto BH is consistent with the light curves of optical/UV TDEs (Mockler et al. 2019). Following Liu et al. (2017), we assume that the eccentricity of the elliptical accretion disks of TDEs is a constant in radius, $e(a) = \text{constant}$, and empirically $e = e_d$. To describe the motions of particles of highly eccentric orbits in the field of Schwarzschild BH, we adopt the generalized Newtonian potential in the low-energy limit (gNR, Tejada & Rosswog 2013)

$$\Phi_G = -\frac{GM_{\text{BH}}}{r} - \left(\frac{2r_g}{r-2r_g}\right) \left[\left(\frac{r-r_g}{r-2r_g}\right) v_r^2 + \frac{1}{2}v_\phi^2 \right], \quad (5)$$

where r_g is the gravitational radius, v_r and v_ϕ are, respectively, the radial and azimuthal velocities of particles. In gNR, the specific binding energy ϵ_G and angular momentum l_G of an elliptical orbit with semimajor axis a and eccentricity e_d are, respectively,

$$\epsilon_G \simeq -\frac{c^2}{2} \frac{r_s[a(1-e_d^2)-2r_s]}{a[2a(1-e_d^2)-(3+e_d^2)r_s]} \quad (6)$$

and

$$l_G \simeq \frac{(1-e_d^2)ac\sqrt{r_s}}{\sqrt{2(1-e_d^2)a-(3+e_d^2)r_s}} \quad (7)$$

(Liu et al. 2017; Cao et al. 2018).

When the disk fluid elements migrate inwards and the pericenter reaches the marginally stable radius r_{ms} , the matter passes through r_{ms} and falls freely onto the BH. The orbit of pericenter at marginally stable radius r_{ms} gives the location of the inner edge of the elliptical accretion disk. The elliptical accretion disk of constant eccentricity e_d has an inner edge $a_{\text{in}} = r_{\text{ms}}/(1-e_d)$. For particles with circular orbits, the marginally stable circular orbit or the innermost stable circular orbit (ISCO) is at $r_{\text{ms}} = 3r_s$, while for particles with parabolic orbits the marginally stable radius is at $r_{\text{ms}} = 2r_s$. For particles of general trajectories of eccentricity $0 < e < 1$, we have the marginally stable radius $2r_s < r_{\text{ms}} < 3r_s$. Provided r_{ms} , equation (6) gives the binding energy of particles at the inner edge of elliptical disk or the conversion efficiency of matter into radiation of elliptical accretion disk

$$\eta \simeq -\frac{\epsilon_G}{c^2} \simeq \frac{1}{2} \frac{r_s[(1+e_d)r_{\text{ms}}-2r_s](1-e_d^2)}{(1+e_d)r_{\text{ms}}[2(1+e_d)r_{\text{ms}}-(3+e_d^2)r_s]}. \quad (8)$$

For $e_d = 1$ and $r_{\text{ms}} = 2r_s$, equation (8) gives $\eta = 0$, as expected for a parabolic orbit. For $e_d = 0$ and $r_{\text{ms}} = 3r_s$, equation (8) gives $\eta \simeq 1/18$, which is about 2.9% smaller than the exact value $\eta \simeq 0.0572$. From equations (8) and (3), we have

$$\begin{aligned} \eta &= \eta_0(1 - e_d^2) \simeq \eta_0 \left[2\delta + \sin^2 \left(\frac{\Omega}{2} \right) \right] = 2\eta_0\delta(1 + \Delta) \\ &\simeq \eta_0 \left\{ 2\delta + \sin^2 \left[\frac{3\pi}{4} \frac{\beta}{(1 - 0.5\delta)} \frac{r_s}{r_t} \right] \right\}, \end{aligned} \quad (9)$$

where

$$\eta_0 = \frac{1}{2} \frac{r_s[(1 + e_d)r_{\text{ms}} - 2r_s]}{(1 + e_d)r_{\text{ms}}[2(1 + e_d)r_{\text{ms}} - (3 + e_d^2)r_s]} \quad (10)$$

depends very weakly on both r_{ms} and e_d . For $e_d = 1$ and $r_{\text{ms}} = 2r_s$ $\eta_0 = 0.0625$, while $\eta_0 = 0.0556$ for $e_d = 0$ and $r_{\text{ms}} = 3r_s$. It is a good approximation to adopt the average $\eta_0 = 0.059$ in the calculation of radiation efficiency with equation (9), especially for $r_p \gg r_s$

$$\eta \simeq 2.36 \times 10^{-3} \left(\frac{\eta_0}{0.059} \right) (1 + \Delta) \beta^{-1} m_*^{1/3} M_6^{-1/3} \quad (11)$$

and $\Delta \simeq 0.25\beta^3 r_*^{-2} m_*^{1/3} M_6^{5/3}$.

Here we give an estimate η_0 with a bit higher accuracy, by calculating the marginally stable radius r_{ms} with the eccentricity given by equation (3). From equation (7), the angular momentum of the fluid elements of the disk inner edge with eccentricity e_d is approximately

$$l_{\text{in}} \simeq \frac{(1 + e_d)r_{\text{ms}}c\sqrt{r_s}}{\sqrt{2(1 + e_d)r_{\text{ms}} - (3 + e_d^2)r_s}}. \quad (12)$$

For fluid elements with specific angular momentum l_{in} , the marginally stable radius is given by

$$l_{\text{in}} = l_{\text{K}} \quad (13)$$

(Abramowicz et al. 1978), where

$$l_{\text{K}} = \Omega_{\text{K}} \frac{r_{\text{ms}}^3}{r_{\text{ms}} - r_s} \quad (14)$$

is the specific angular momentum of the Keplerian circular motion and $\Omega_{\text{K}} = (GM_{\text{BH}}/r_{\text{ms}}^3)^{1/2}$ is the Keplerian angular velocity. From equations (12), (13), and (14), we obtain the marginally stable radius

$$r_{\text{ms}} = \frac{A}{4(1 + e_d)e_d} r_s, \quad (15)$$

where $A = 1 + 8e_d + 3e_d^2 + \sqrt{1 + 22e_d^2 - 7e_d^4}$ increases with the decrease of eccentricity. For $e_d = 1$, equation (15) give $r_{\text{ms}} = 2r_s$ consistent with the marginally bound radius of parabolic orbits. When $e_d \leq 0.406$, equation (15) gives $r_{\text{ms}} \geq 3r_s$. In the calculation of the efficiency η , $r_{\text{ms}} = 3r_s$ is adopted for eccentricity $e_d \leq 0.406$.

We notice that in equation (9) $\eta_0 \simeq 0.059$ is about the radiation efficiency of the standard thin accretion disk in Schwarzschild black hole and the radiation efficiency η of elliptical accretion disk of TDEs is the typical radiation efficiency of standard thin accretion disk modified by a factor $(1 - e^2)$. Equation (9) shows

that the radiation efficiency of elliptical accretion disk of TDEs strongly depends both on the masses of BH and star and on the orbital penetration factor of star. Figure 1 shows the conversion efficiency of matter into radiation η as a function of masses of BH and star. To obtain Figure 1, we have used the mass-radius relations of main sequence stars and BDs to calculate the radius with mass. The results of two typical orbital penetration factors, $\beta = 1$ and 2, are given. Figure 1 show that the radiation efficiency of elliptical accretion disk is a complicated strong function of BH mass of deep minimum, as low as $\eta \sim 10^{-3}$. The location of the minimum of the efficiency depends on the mass and orbital penetration factor of star: a higher stellar mass shifts the curves and locations of minimum to a higher BH mass and meanwhile increase the minimum of the efficiency. However, the increase of penetration factor mainly shifts the curves toward smaller BHs. Figure 1 plots the typical radiation efficiency $\eta = 0.1$ always adopted for TDEs and AGNs in the literature for comparison. The radiation efficiency of elliptical accretion disk is significantly smaller than the typical efficiency $\eta = 0.1$. For example, the radiation efficiency of TDEs with solar-type star by BH of mass $10^6 M_\odot$ is about $10^{-2.5}$, about 30 times smaller than the typical efficiency of AGNs.

3. PEAK LUMINOSITIES AND TOTAL RADIATION ENERGY AFTER PEAK

The peak luminosities of light curves and the total radiation energy or the accreted stellar masses can be determined observationally. We calculate the expectations of the elliptical accretion disk model in this section and compare them to the observations of TDEs in next section.

Analytic and hydrodynamic simulations of tidal disruptions of star show that the fallback rate of the bound stellar debris after peak can be well approximated with a power-law in time

$$\dot{M} \simeq \dot{M}_p \left(\frac{t - t_d}{\Delta t_p} \right)^{-n} \quad (16)$$

for $t \geq t_p$, where $\Delta t_p = t_p - t_d$ with t_d and t_p , respectively, the time of tidal disruption and peak mass accretion rate, power-law index n of typical value $n = 5/3$ is a constant depending on the structure and age of star (Lodato et al. 2009; Guillochon & Ramirez-Ruiz 2013; Golightly et al. 2019; Law-Smith et al. 2019; Ryu et al. 2019), and \dot{M}_p is the peak mass fallback rate

$$\dot{M}_p \simeq A_\gamma r_*^{-3/2} m_*^2 M_6^{-1/2} M_\odot / \text{yr}, \quad (17)$$

where A_γ is a constant depending on the penetration factor β and the structure and age of star (Lodato et al. 2009; Guillochon & Ramirez-Ruiz 2013; Golightly et al. 2019; Law-Smith et al. 2019; Ryu et al. 2019). For tidal disruption of a solar-type star with polytropic index $\gamma = 5/3$ and penetration factor $\beta = 1$, we have $n \simeq 5/3$ and $A_{5/3} \simeq 1.328$ (Guillochon & Ramirez-Ruiz 2013). For tidal disruptions of stars with different masses, we adopted the results of the hydrodynamic simulations of polytropic stars (Guillochon & Ramirez-Ruiz 2013). We adopted the polytropic models with $\gamma = 5/3$ both for brown dwarfs with mass between $0.01 M_\odot$ and $0.08 M_\odot$ (Chabrier & Baraffe 2000) and low mass main sequence stars with mass between $0.08 M_\odot$ and $1 M_\odot$, and with $\gamma = 4/3$ for high mass stars with mass $M_* > 20 M_\odot$. For stars with mass between $1 M_\odot$ and $20 M_\odot$, we use a hybrid model obtained by linearly interpolating the results of hydrodynamic simulations of polytropes with indices $\gamma = 5/3$ and $\gamma = 4/3$. No hydrodynamic simulation of tidal disruptions of brown dwarfs are carried out in the literature. Because the degeneracy of electron gas affects the equation of state (EOS) of brown dwarfs and the degenerate electron gas could be described by polytropes of index $\gamma = 5/3$ (Chabrier & Baraffe 2000), we extrapolate the results of tidal disruptions of brown dwarfs with the hydrodynamic simulations of the low-mass stars with polytropic index $\gamma = 5/3$ (Guillochon & Ramirez-Ruiz 2013).

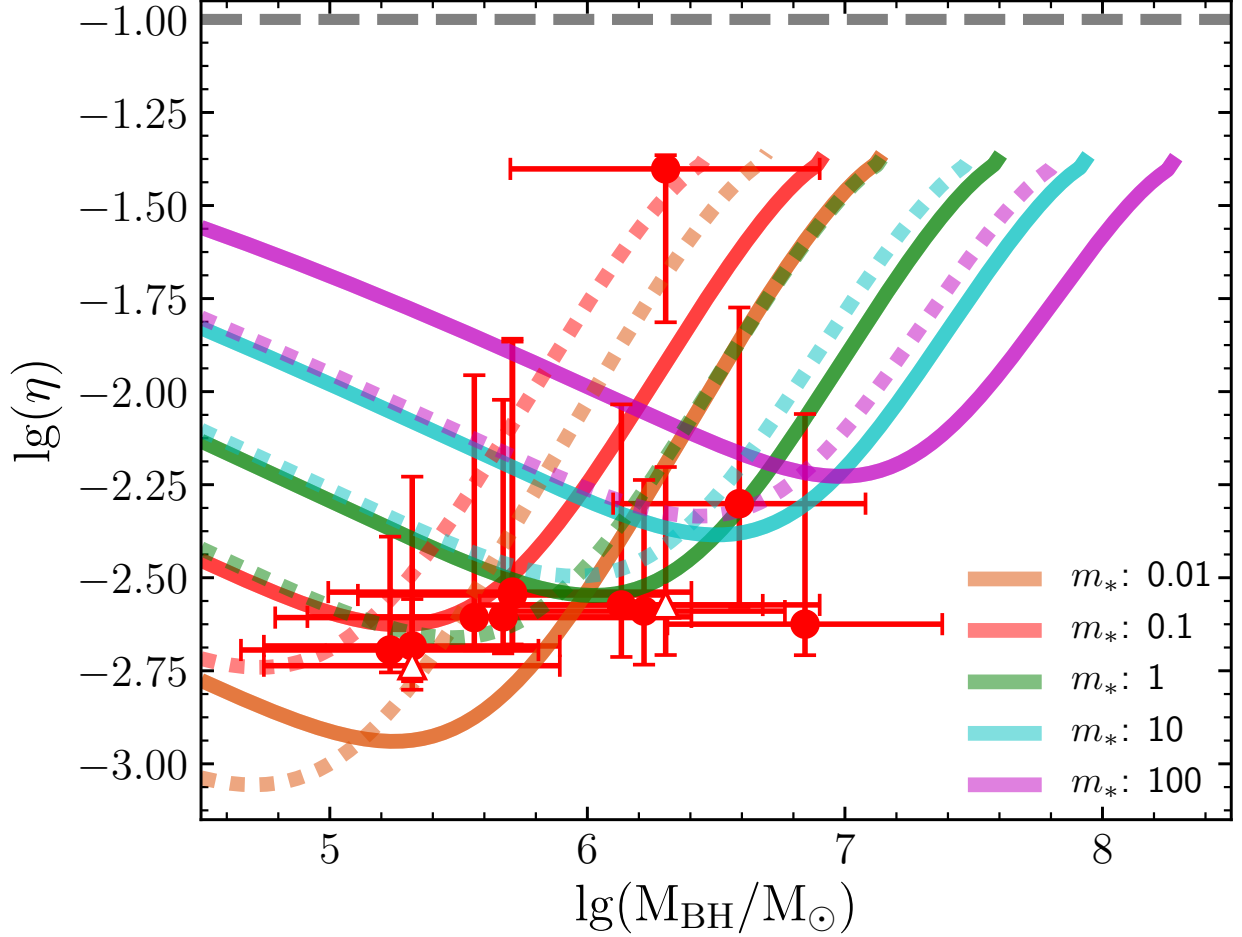


Figure 1. Radiation efficiency vs BH mass for different stellar mass. Solid and dotted lines are, respectively, for $\beta = 1$ and $\beta = 2$. Gray dashed line is for $\eta = 0.1$. Radiation efficiency decreases with BH mass until the minimum and increases afterwards, while it increases with stellar mass for BH mass before minimum and decrease with stellar mass afterwards. The BH mass of minimum radiation efficiency increases with stellar mass. Filled circles are the radiation efficiency and associated uncertainties at 90% level of the sample TDE sources in Table 2. Open triangle is for the secondary solutions of TDEs.

For the typical radiation efficiency $\eta = 0.1$ of circular accretion disk, equation (17) gives the peak luminosity

$$\begin{aligned}
 L_p &= \eta \dot{M}_p c^2 \\
 &\simeq 7.53 \times 10^{45} \text{ erg s}^{-1} \left(\frac{A_\gamma}{1.328} \right) M_6^{-1/2} r_*^{-3/2} m_*^2 \\
 &\simeq 60 L_{\text{Edd}} \left(\frac{A_\gamma}{1.328} \right) M_6^{-3/2} r_*^{-3/2} m_*^2
 \end{aligned} \tag{18}$$

with $L_{\text{Edd}} = 1.25 \times 10^{44} M_6 \text{ erg s}^{-1}$ the Eddington luminosity is super-Eddington for BH of mass $M_{\text{BH}} \lesssim 1.5 \times 10^7 (A_\gamma/1.328)^{2/3} r_*^{-1} m_*^{4/3} M_\odot$. Because the peak luminosity is highly super-Eddington, the light curves of TDEs for BH mass $M_{\text{BH}} \sim 10^6 M_\odot$ is Eddington-limited and should deviate from the fallback rate given with equation (16). For elliptical accretion disk with efficiency given by equation (9), the peak luminosity

of TDEs is

$$\begin{aligned}
 L_p &= \eta \dot{M}_p c^2 \\
 &= \eta_0 A_\gamma \left[2\delta + \sin^2 \left(\frac{\Omega}{2} \right) \right] r_*^{-3/2} m_*^2 M_6^{-1/2} c^2 M_\odot / \text{yr} \\
 &\simeq 1.78 \times 10^{44} \text{ erg s}^{-1} \left(\frac{\eta_0}{0.059} \right) \left(\frac{A_\gamma}{1.328} \right) \beta^{-1} r_*^{-3/2} m_*^{7/3} M_6^{-5/6} \times \\
 &\quad \left(1 + 0.25 \beta^3 r_*^{-2} m_*^{1/3} M_6^{5/3} \right). \tag{19}
 \end{aligned}$$

In equation (19), the last equality is valid for $r_p \gg r_s$. Equation (19) shows that the peak luminosity of TDEs is sub-Eddington for TDEs with BH mass $M_{\text{BH}} \gtrsim 10^6 M_\odot$ and the light curves are expected to follow the fallback rate of bound stellar debris. The peak luminosity is significantly super-Eddington and a Eddington-limited peak brightness is expected only for TDEs with BH mass $M_{\text{BH}} \ll 1.2 \times 10^6 M_\odot (\eta_0/0.059)^{6/11} (A_\gamma/1.328)^{6/11} \beta^{-6/11} r_*^{-9/11} m_*^{14/11}$, about an order of magnitude smaller than that suggested by equation (18). The peak accretion rate is super-Eddington only for BH mass $M_{\text{BH}} \lesssim 5.7 \times 10^5 M_\odot (\eta_0/0.059)^{6/11} (A_\gamma/1.328)^{6/11} \beta^{-6/11}$ when the disrupted star is a late-type M-dwarf with typical mass $m_* \simeq 0.3$. For massive BH with mass $M_{\text{BH}} \gtrsim 10^6 M_\odot$ to produce a TDE with significantly super-Eddington luminosity, the disrupted star must be a B- or O-type star. Our results predict that TDEs whose light curves clearly shows Eddington-limited luminosity would predominantly occur in either dwarf galaxies with intermediate mass BH or star-forming galaxies and avoid occurring in quiescent galaxies.

Equation (18) shows that in circular accretion disk the peak luminosity increases with BH mass as $L_p \sim L_{\text{Edd}} \propto M_{\text{BH}}$ for $M_{\text{BH}} \lesssim 2 \times 10^7 M_\odot$ because of Eddington-limitation and decreases with BH mass $L_p \propto M_{\text{BH}}^{-1/2}$ for $M_{\text{BH}} \gtrsim 2 \times 10^7 M_\odot$. A peak of the distribution of peak luminosity would expected at $M_{\text{BH}} \sim 2 \times 10^7 M_\odot$. While, in the elliptical disk, equation (19) shows that the peak luminosity decreases with BH mass as $L_p \propto M_{\text{BH}}^{-5/6}$ for $M_{\text{BH}} \lesssim 2 \times 10^6 M_\odot \beta^{-9/5} r_*^{6/5} m_*^{-1/5}$ but increases with BH mass as $L_p \propto M_{\text{BH}}^{5/6}$ for $M_{\text{BH}} \gtrsim 3 \times 10^6 M_\odot \beta^{-9/5} r_*^{6/5} m_*^{-1/5}$. A minimum of the distribution of peak luminosity is prominent in Figure 2, and the BH mass at minimum increases with stellar mass for main-sequence stars and decrease with stellar mass for brown dwarfs. The upper panel of Figure 2 gives the expected peak luminosity of the elliptical disk model as a function of the masses of BHs and stars for penetration factor $\beta = 1$. To obtain Figure 2, we have used the mass-radius relations to calculate the radii with masses of stars and brown dwarfs. The ranges of masses of different types of stars are taken from Cox (2000). Figure 2 shows that the peak luminosities of TDEs strongly depends on both the BH and stellar masses and increase monotonically with the mass of stars except at the transitions from BDs to late M-type main sequences and from F-type to early O-type main sequences. In Figure 2, we also plot the peak luminosity as a function of BH mass given with equation (18) for $\eta = 0.1$ and $M_* = M_\odot$. Figure 2 shows that for TDEs with solar-type star the peak luminosities expected with the popular circular accretion disk model in the literature is typically orders of magnitude higher than those expected with the elliptical accretion disk model.

From equation (16), the total fallback and accreted mass after peak time t_p is

$$\begin{aligned}
 \Delta M_* &\simeq \int_{t_p}^{\infty} \dot{M}_p \left(\frac{t-t_d}{t_p-t_d} \right)^{-n} dt \simeq \frac{\dot{M}_p}{n-1} \Delta t_p \\
 &\simeq \frac{A_\gamma B_\gamma}{n-1} m_* M_\odot \simeq \frac{3}{2} A_\gamma B_\gamma m_* M_\odot \tag{20}
 \end{aligned}$$

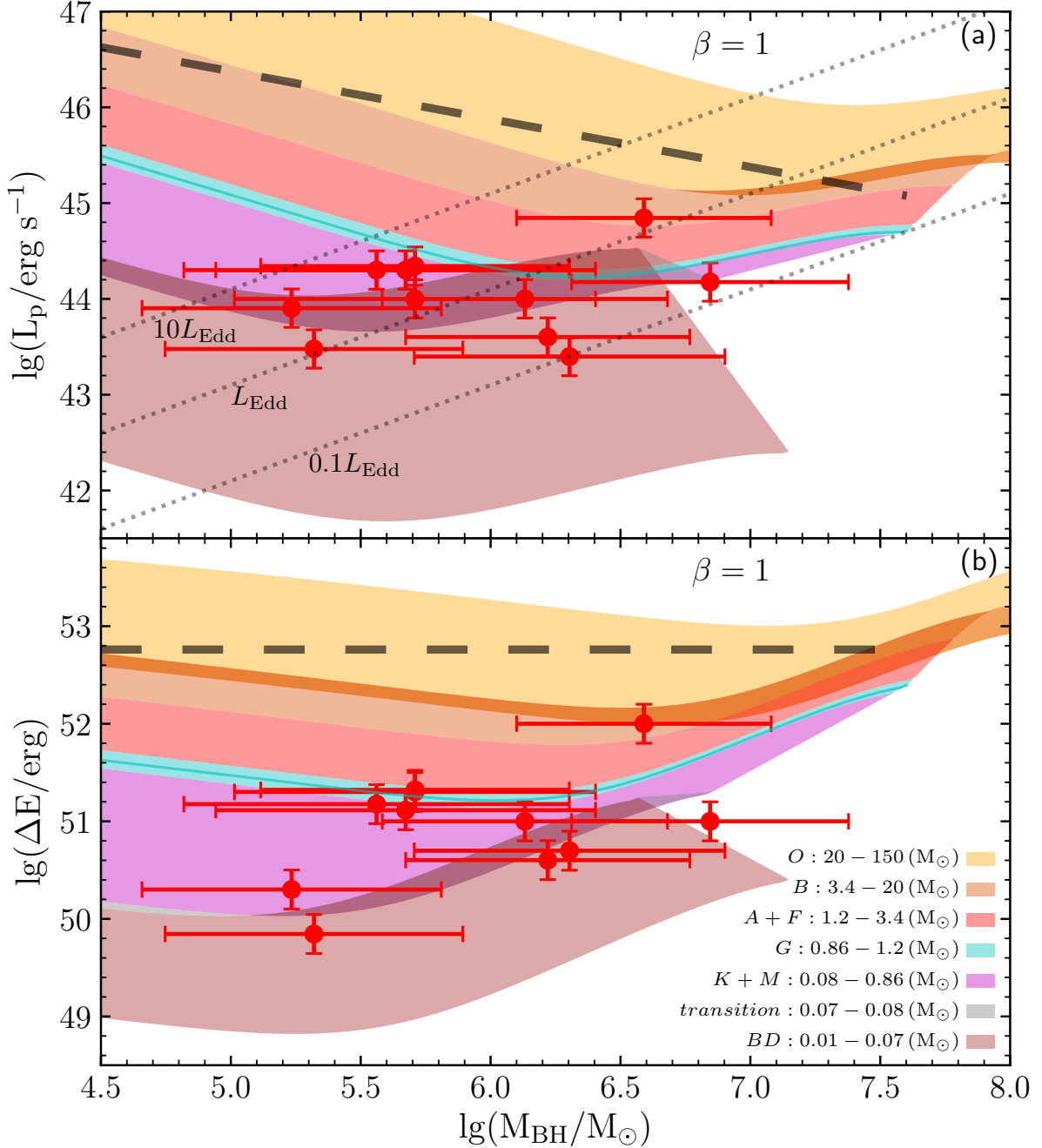


Figure 2. Peak luminosity (*upper*) and total radiation energy after peak (*lower*) vs BH mass. The mass ranges of stellar spectral types are adopted from Cox (2000) and coded with colors. Thick dashed and thin solid lines are for the L_{p} (*upper*) and ΔE (*lower*) expected, respectively, with the radiation efficiency $\eta = 0.1$ and with the elliptical disk model for one solar mass star. Distributions are truncated at BH mass where tidal radius $r_{\text{t}} = r_{\text{ms}}$. Filled circles give the observations of the TDE sample sources with BH masses calculated with the $M_{\text{BH}} - \sigma_{*}$ relation.

where $\Delta t_{\text{p}} = t_{\text{p}} - t_{\text{d}} \simeq B_{\gamma} M_6^{1/2} m_*^{-1} r_*^{3/2}$ yr is the time of peak accretion and B_{γ} is a constant depending on the polytropic index γ and the orbital penetration factor β of star (Guillochon & Ramirez-Ruiz 2013). To obtain the last equality in equation (20), we have adopted the typical value $n = 5/3$. For $\gamma = 5/3$ and $\beta = 1$, we have $B_{5/3} = 0.1618$ from the appendix of Guillochon & Ramirez-Ruiz (2013). Equation (20) gives the expected

total accreted stellar mass $\Delta M_* \simeq 0.322(A_\gamma B_\gamma/0.215)m_* M_\odot$ after the peak time of light curves. For a circular accretion disk of typical conversion efficiency $\eta = 0.1$, the total accreted mass gives the expected total radiation energy $\Delta E = \eta \Delta M_* c^2 \simeq 5.76 \times 10^{52} \text{ erg } (A_\gamma B_\gamma/0.215)m_*$, which depends only on the mass of star in a full disruption and is independent of BH mass. For a typical star of mass $M_* = 0.3M_\odot$, the expected total energy of radiation is $\Delta E \simeq 1.73 \times 10^{52} \text{ erg } (A_\gamma B_\gamma/0.215)$.

For the elliptical accretion disk with radiation efficiency given by equation (9), equation (20) gives the total energy of radiation

$$\begin{aligned} \Delta E &\simeq \eta \Delta M_* c^2 \\ &\simeq \frac{\eta_0}{n-1} \left[2\delta + \sin^2 \left(\frac{\Omega}{2} \right) \right] A_\gamma B_\gamma m_* M_\odot c^2 \\ &\simeq 1.36 \times 10^{51} \text{ erg } \left(\frac{\eta_0}{0.059} \right) \left(\frac{A_\gamma B_\gamma}{0.215} \right) \beta^{-1} m_*^{4/3} M_6^{-1/3} \times \\ &\quad \left(1 + 0.25 \beta^3 r_*^{-2} m_*^{1/3} M_6^{5/3} \right), \end{aligned} \quad (21)$$

which depends not only on the mass of star but also on the BH mass and orbital penetration factor of star. It is about 34 and 7 times smaller than the total radiation energy expected with the typical efficiency $\eta = 0.1$, respectively, for TDEs with tidal disruption of solar-type star by BH masses $M_{\text{BH}} = 10^6 M_\odot$ and $10^7 M_\odot$. The big differences of total radiation energy expected with the two kinds of accretion disk models implies that the missing energy problem raised in the literature of TDEs may be due to the adopt of the large radiation efficiency by assuming a circular accretion disk model as an analogy of AGNs. No missing energy problem would be expected with the elliptical accretion disk model. It will be discussed further in Sec. 4. The lower panel of Figure 2 presents the expected total emitted energy as a function of masses of BH and star for orbital penetration factor $\beta = 1$. In Figure 2, we also plot the expected total radiation energy computed for TDEs of a solar-type star with the typical radiation efficiency $\eta = 0.1$. Provided the mass of star, the expected total emitted energy weakly decreases with BH mass $\Delta E \propto M_{\text{BH}}^{-1/3}$ until $M_{\text{BH}} \sim 2 \times 10^6 M_\odot \beta^{-9/5} r_*^{6/5} m_*^{-1/5} \sim 2 \times 10^6 M_\odot \beta^{-9/5} m_*^{1-1.2\zeta}$ and significantly increases when $M_{\text{BH}} \gtrsim 3 \times 10^6 M_\odot \beta^{-9/5} r_*^{6/5} m_*^{-1/5} \sim 3 \times 10^6 M_\odot \beta^{-9/5} m_*^{1-1.2\zeta}$. The change occurs at the mass of BH $M_{\text{BH}} \sim 3 \times 10^6 M_\odot \beta^{-9/5} m_*^{1-1.2\zeta}$ with $\zeta = 0.21$ for $0.08 < m_* \leq 1$ and $\zeta = 0.44$ for $1 < m_* \leq 150$.

From the total radiation energy given with equation (21), we can calculate the expected accreted stellar mass to power a TDE with the canonical radiation efficiency $\eta = 0.1$,

$$\begin{aligned} \Delta M_{\text{app}} &= \frac{\Delta E}{0.1 c^2} = \left(\frac{\eta}{0.1} \right) \Delta M_* \\ &\simeq 15 \eta_0 \left[2\delta + \sin^2 \left(\frac{\Omega}{2} \right) \right] A_\gamma B_\gamma m_* M_\odot, \end{aligned} \quad (22)$$

which for $r_p \gg r_s$ gives

$$\begin{aligned} \Delta M_{\text{app}} &\simeq 7.61 \times 10^{-3} M_\odot \left(\frac{\eta_0}{0.059} \right) \left(\frac{A_\gamma B_\gamma}{0.215} \right) \beta^{-1} m_*^{4/3} M_6^{-1/3} \times \\ &\quad \left(1 + 0.25 \beta^3 r_*^{-2} m_*^{1/3} M_6^{5/3} \right) \end{aligned} \quad (23)$$

Equations (22) and (23) show that the expected accreted stellar mass needed to power a TDE is only a very small fraction of solar mass and is about 34 times and 7 times smaller than the real accreted stellar mass

ΔM_* , respectively, for BH mass $M_{\text{BH}} = 10^6 M_\odot$ and $10^7 M_\odot$. The results suggest that the observations of the low accreted stellar matter of TDEs in the literature is due to the use of canonical radiation efficiency $\eta = 0.1$ and is only an observational effect. Therefore, we would call it the apparent accreted stellar mass. The apparent accreted stellar mass after peak is $\Delta M_{\text{app}} \simeq 0.045 M_\odot$ from Equation (23) or $0.04 M_\odot$ from Equation (22) for $M_{\text{BH}} = 10^7 M_\odot$ and $M_* = 1 M_\odot$. The apparent accreted stellar mass is $\Delta M_{\text{app}} \simeq 3 \times 10^{-3} M_\odot$ and $7 \times 10^{-4} M_\odot$, respectively, for tidal disruptions of M star with mass $M_* = 0.3 M_\odot$ and brown dwarf with mass $0.03 M_\odot$ by BH of mass $10^6 M_\odot$.

Equations (19) and (21) show that both the peak luminosity and the total radiation energy depend on the masses of the BH and star and also the orbital penetration factor β . Because A_γ and B_γ depend very weakly on β for $\beta \gtrsim 0.9$, the peak luminosity L_p and the total radiation energy ΔE depend on β mainly because of the radiation efficiency η . For tidal disruption with $\Delta = 0.25 \beta^3 r_*^{-2} m_*^{1/3} M_6^{5/3} \lesssim 1$, or with $\beta \lesssim 2.1$ and $M_{\text{BH}} \lesssim 10^{6.5} M_\odot$, we have $L_p \sim \beta^{-1} (1 + \Delta) m_*^{(5+9\zeta)/6} M_6^{-5/6} \sim \beta^{-1} (1 + \Delta) m_*^{1.15} M_6^{-5/6}$ and the total radiation energy $\Delta E \sim \beta^{-1} (1 + \Delta) m_*^{4/3} M_6^{-1/3}$ for $\zeta = 0.21$, both of which are nearly independent of the orbital penetration factor because $1.2 \lesssim \beta^{-1} (1 + \Delta) \lesssim 1.6$ (or varying by only about 30%) for $0.7 \lesssim \beta \lesssim 2.1$. Provided L_p and ΔE , we can uniquely determine the masses of star and BHs but give only poor observational constraints of the penetration factor for TDEs of shallow orbital pericenter penetration $\beta \sim 1$, with which most TDEs are expected to occur. While for tidal disruption with $\Delta \gg 1$ (either $\beta \gtrsim 2.5$, $m_* \lesssim 0.11$, or $M_{\text{BH}} \gtrsim 10^{6.7} M_\odot$), we have the peak luminosity $L_p \sim \beta^2 m_*^{(-5+21\zeta)/6} M_6^{5/6} \sim \beta^2 m_*^{-0.098} M_6^{5/6}$ and the total radiation energy $\Delta E \sim \beta^2 m_*^{(-1+6\zeta)/3} M_6^{4/3} \sim \beta^2 m_*^{0.087} M_6^{4/3}$, both of which are strongly depends on the penetration factor and BH mass but nearly independent of the mass of the disrupted star. Provided L_p and ΔE , we can uniquely determine the mass of BH and the orbital penetration factor but not the mass of star. The above analyses show that the BH mass of TDEs can be always well determined from the observations of L_p and ΔE . However, the mass of disrupted star and the orbital penetration factor cannot be determined simultaneously: the mass of the disrupted star can be uniquely determined for TDEs with negligible relativistic apsidal precession of the most bound stellar debris with $\Delta \lesssim 1$, or the penetration factor β can be well determined observationally if the relativistic apsidal precession of the most bound stellar debris of TDE is significant with $\Delta \gg 1$.

4. CONFRONTATION WITH THE OBSERVATIONS

In section 3, we calculated the expected peak luminosities and total radiation energy after peak of TDEs with the elliptical accretion disk model. In this section, we compare the expectations to the observations of the peak luminosities and total radiation energy of TDEs. We adopt a Λ CDM cosmology with $H_0 = 70 \text{ km s}^{-1} \text{ Mpc}^{-1}$, $\Omega_M = 0.3$ and $\Omega_\Lambda = 0.7$ when it needs.

4.1. The observational data

Among the known 30-60 TDEs and candidates¹ (Komossa 2015), some of them have well observed peaks of light curves and can be used in the comparison of the expectations of the elliptical accretion disk and the observations of the peak luminosity and total radiation energy of TDEs. Because we are interested only in the energy released by the accretion disk formed at tidal disruption of star, a TDE is included in the sample source only when (1) it is not relativistically jetted, (2) the host galaxy does not show any permanent AGN activity, (3) the peak of brightness is well detected, and (4) the location is in coincidence with the nucleus of host galaxy. The brightness peak of light curve is well detected, if the observational time gap neither before

¹ An *Open TDE Catalog* is available at <https://tde.space>

Table 1. The sample sources

Name	z	Type	Ref.	σ_*	Ref.	$\lg(M_{\text{BH},\sigma})$	$\lg(M_{\text{tot}})$	Ref.	$\lg(M_{\text{BH,tot}})$	B/T ^a	Lp	Ref.	ΔE	Ref.
(1)	(2)	(3)	(4)	(5)	(6)	(7)	(8)	(9)	(10)	(11)	(12)	(13)	(14)	(15)
				(km s ⁻¹)		(M _⊙)	(M _⊙)		(M _⊙)		(10 ⁴⁴ erg s ⁻¹)		(10 ⁵⁰ erg)	
iPTF16fnl	0.0163	Opt./UV	1,2	55±2	3	5.32 ^{+0.57} _{-0.58}	9.8	4	6.19±0.55	0.29	0.3	2	0.7 ^b	2
ASASSN-14li	0.0206	Opt./UV	5	78±2	3	6.13 ^{+0.55} _{-0.55}	9.6	4	5.98±0.55	0.22	1	5,7	10 ^b	5,7
ASASSN-14ae	0.0436	Opt./UV	8	53±2	3	5.23 ^{+0.58} _{-0.58}	9.8	4	6.19±0.55	0.29	0.8	8	2 ^b	8
ASASSN-15oi	0.0479	Opt./UV	9	61±7	10	5.56 ^{+0.74} _{-0.77}	9.9	4	6.30±0.55	0.34	2	11	15 ^b	11
PTF09ge	0.064	Opt./UV	12	81±2	3	6.22 ^{+0.55} _{-0.55}	10.1	4	6.51±0.55	0.44	0.4	13	4 ^b	13
iPTF15af	0.07897	Opt./UV	14	106±2	3	6.85 ^{+0.53} _{-0.53}	10.2	4	6.61±0.55	0.47	1.5	14	10 ^b	14
SDSS J0952+2143	0.079	Opt./UV	15	95	15	6.59 ^{+0.49} _{-0.49}	10.37	16	6.79±0.55	0.53	7	17	100 ^b	17
PS1-10jh	0.1696	Opt./UV	18	65±3	3	5.71 ^{+0.59} _{-0.60}	9.5	4	5.88±0.55	0.19	2.2	18	21	18
PTF09djl	0.184	Opt./UV	12	64±7	3	5.67 ^{+0.73} _{-0.76}	10.1	4	6.51±0.55	0.44	2	13	13 ^b	13
GALEX D23H-1	0.1855	Opt./UV	19	84±4	10	6.30 ^{+0.60} _{-0.60}	10.3	4	6.72±0.55	0.51	0.25	19	5 ^b	19
GALEX D11-9	0.326	Opt./UV	20	65±6	10	5.71 ^{+0.70} _{-0.72}	10.3	4	6.72±0.55	0.51	1	20	20 ^b	20
XMMSL1 J0740	0.0173	X-ray	21	~ 10.62 ^c	...	7.05±0.55	0.60	2	21	6 ^b	21
AT2018dyb	0.0180	Opt./UV	22	10.08	22	6.48±0.55	0.43	1.3	22	8 ^b	22
ASASSN-19bt	0.0262	Opt./UV	23	10.04	23	6.44±0.55	0.41	1.3	23	10 ^b	23
AT2018fyk	0.059	Opt./UV	24	10.2	24	6.61±0.55	0.47	3	24	30 ^b	24
PS18kh	0.071	Opt./UV	25,26,27	10.15	25	6.55±0.55	0.46	0.9	25	7 ^b	25
AT2017eqx	0.1089	Opt./UV	28	9.36	28	5.73±0.55	0.14	1	28	4 ^b	28
PS1-11af	0.4046	Opt./UV	29	10.1	4	6.51±0.55	0.44	0.8	29	6 ^b	29

NOTE—The sample sources are divided into two groups: the upper part of the table for the sample sources with the observations of the stellar velocity dispersions of host galaxies and the lower part for sample sources without the observations.

^a The bulge-to-total ratio (B/T) is estimated with an empirical relation between B/T and the total stellar mass of galaxy (Stone et al. 2018). It is obtained by averaging the B/T for different total stellar mass bin and has a very large uncertainty because B/T varies from less than 0.1 to about 0.7 for late-type galaxy (Gao et al. 2019).

^b The energy from the literature indicates only the radiated energy over the period of observational campaign, and is corrected to infinity.

^c The total stellar mass is estimated with the 2MASS apparent K-band magnitude $K = 10.96$ (Saxton et al. 2017) and the average stellar mass-to-light ratio (M/L) (Bell et al. 2003). This is only a rough estimate as we lack the host color information.

References—¹Blagorodnova et al. (2017), ²Brown et al. (2018), ³Wevers et al. (2017), ⁴van Velzen (2018), ⁵Holoien et al. (2016a), ⁶French et al. (2017), ⁷Brown et al. (2017), ⁸Holoien et al. (2014), ⁹Holoien et al. (2016b), ¹⁰Wevers et al. (2019b), ¹¹Holoien et al. (2018), ¹²Arcavi et al. (2014), ¹³van Velzen et al. (2019b), ¹⁴Blagorodnova et al. (2019), ¹⁵Komossa et al. (2008), ¹⁶Graur et al. (2018), ¹⁷Palaversa et al. (2016), ¹⁸Gezari et al. (2012), ¹⁹Gezari et al. (2009), ²⁰Gezari et al. (2008), ²¹Saxton et al. (2017), ²²Leloudas et al. (2019), ²³Holoien et al. (2019b), ²⁴Wevers et al. (2019a), ²⁵Holoien et al. (2019a), ²⁶van Velzen et al. (2019a), ²⁷Hung et al. (2019), ²⁸Nicholl et al. (2019), ²⁹Chornock et al. (2014)

nor after the maximum luminosity of the light curve of a TDE is larger than 30 days in the rest frame of the source. We adopted 30 days as the upper limit of the observational time gap because the time of peak accretion of a TDE of a solar-type star by BH of mass $10^6 M_{\odot}$ is $\Delta t_p \simeq 59$ days. The last requirement is adopted in order that the BH mass can be calculated with the empirical $M_{\text{BH}}-\sigma_*$. Based on the requirement, the TDE candidates ROTSE *Dougie* and AT2018cow are not one of the sample sources because they have off-nuclear locations, although the peaks of the light curves have been well detected (Vinkó et al. 2015; Kuin et al. 2019; Margutti et al. 2019; Perley et al. 2019).

The 18 sample sources are identified and given in Table 1. All the sample sources except ASASSN-14li and SDSS J0952+2143 have well observed peaks of light curves at the wavebands of discovery. The peak brightness of light curves of TDE ASASSN-14li cannot be constrained in the optical/UV waveband of discovery because the observational time gap before the first detection of the event of 2014 November 11 is 121-days in the observer frame or 118.6 days in the source frame (Holoien et al. 2016b), but be well detected

in the soft X-ray waveband (Miller et al. 2015; Brown et al. 2017; Bright et al. 2018). TDE candidate SDSS J0952+2143 was discovered with the detection of transient ultra-strong optical emission lines during the spectral SDSS observations (Komossa et al. 2008) and has an unfiltered optical light curve from the Lincoln Near Earth Asteroid Research (LINEAR) survey (Palaversa et al. 2016). In Table 1, the sample sources are divided into two groups, one with and the other without observations of stellar velocity dispersion of host galaxies. The BH masses of TDEs are calculated with the empirical relation of BH mass and stellar velocity dispersion of bulge, namely the $M_{\text{BH}} - \sigma_*$ relation.

Columns 1 and 2 of Table 1 give the names and redshifts of TDEs. The sample sources are listed according to the increase of redshift. Columns 3 and 4 are the waveband and references of discovery, respectively. Columns 5 and 6 give the host stellar velocity dispersions and the references. Both the luminosity-weighted and central line-of-sight velocity dispersions of most of the TDE sample sources are measured in the literature and have no significant difference (Wevers et al. 2017, 2019b). The measurements of the stellar velocity dispersions in Table 1 are not affected significantly by the disk of host galaxy. Column 7 gives the BH mass obtained with the host stellar velocity dispersion in Col. 5 by the $M_{\text{BH}} - \sigma_*$ relation. Extensive works on the $M_{\text{BH}} - \sigma_*$ relation have been published in the literature and indicate that the $M_{\text{BH}} - \sigma_*$ relation depend on both the type of host galaxy and the range of BH mass of sample sources (e.g. Kormendy & Ho 2013). Because TDEs are expected to occur in all types of galaxies, the $M_{\text{BH}} - \sigma_*$ relations obtained neither with the early- nor late -type galaxies can give good estimates of the black hole masses of TDEs. We estimate the black hole masses with the $M_{\text{BH}} - \sigma_*$ relations obtained with all types of galaxies (Gebhardt et al. 2000; Ferrarese & Merritt 2000; Ferrarese & Ford 2005; Graham et al. 2011; McConnell & Ma 2013; van den Bosch 2016; She et al. 2017). Because the early- and late-type galaxies have their own $M_{\text{BH}} - \sigma_*$ relations with different slopes and zero points, the obtained $M_{\text{BH}} - \sigma_*$ relation depends on the distributions of black hole mass of the sub-sample galaxies. With the tabulated data of all types of galaxies (Kormendy & Ho 2013), She et al. (2017) obtained the relation $\lg(M_{\text{BH}}/M_{\odot}) = (8.32 \pm 0.05) + (5.20 \pm 0.37)\lg(\sigma_*/200\text{ km s}^{-1})$ with an intrinsic scatter of 0.44 dex. Because most TDEs are expected to be caused by a BH of mass less than $10^8 M_{\odot}$, here we calculate the BH masses with the $M_{\text{BH}} - \sigma_*$ relation, $\lg(M_{\text{BH}}/M_{\odot}) = (8.32 \pm 0.04) + (5.35 \pm 0.23)\lg(\sigma_*/200\text{ km s}^{-1})$ with the intrinsic scatter of 0.49 ± 0.03 dex (van den Bosch 2016), which are consistent with the results obtained by She et al. (2017) (with differences $\Delta \lg(M_{\text{BH}}/M_{\odot})$ ranging from 0.04 for $\sigma_* = 110\text{ km s}^{-1}$ to 0.08 for $\sigma_* = 55\text{ km s}^{-1}$) but obtained with twice as large as most previously studied samples and many more low mass objects. The uncertainties of the BH mass in Table 1 include both the observational uncertainties of stellar velocity dispersion and the intrinsic scatter of the $M_{\text{BH}} - \sigma_*$ relation. Although TDEs can occur in all types of galaxies, the spectroscopical observations show that the host galaxies of most known TDEs are E+A or post-starburst galaxies (Arcavi et al. 2014; French et al. 2016). Post-starburst galaxies are in transition between star-forming spirals and passive early-type galaxies and no $M_{\text{BH}} - \sigma_*$ relation specifically for post-starburst galaxies is available in the literature. We may estimate the black hole mass of post-starburst galaxies by averaging the estimates of black hole mass obtained separately with the $M_{\text{BH}} - \sigma_*$ relations for early- and late-type galaxies. By averaging the $M_{\text{BH}} - \sigma_*$ relations given for early- and late-type galaxies (McConnell & Ma 2013), we obtain the interpolation $M_{\text{BH}} - \sigma_*$ relation for TDEs,

$$\lg(M_{\text{BH}}/M_{\odot}) = 8.23 + 5.13\lg(\sigma_*/200\text{ km s}^{-1}). \quad (24)$$

The $M_{\text{BH}} - \sigma_*$ relation given by equation (24) would be nearly independent of the distributions of black hole mass of the sub-sample galaxies.

It was recently suggested that the BH mass may correlate with the total stellar mass of host galaxy (Reines & Volonteri 2015). The relation of BH and total galactic stellar masses obtained from the AGN sample has

been used to estimate the BH masses of TDEs in the literature (e.g. Gezari et al. 2017; Lin et al. 2017b; Holoien et al. 2018; Saxton et al. 2019; Wevers et al. 2019b; Leloudas et al. 2019). Columns 8 and 9 list the total stellar mass of the host galaxy and the reference and Column 10 is the BH mass estimated with the $M_{\text{BH}}-M_{\text{tot}}$ relation, $\lg(M_{\text{BH}}/M_{\odot}) = 7.45 + 1.05 \lg(M_{\text{tot}}/10^{11}M_{\odot})$ (Reines & Volonteri 2015). When more than one measurement of the total stellar mass of host galaxy of TDE are available in the literature, we arbitrarily adopted one of them in the calculations. For XMMSL1 J0740, no measurement of the total stellar mass of host galaxy is available in the literature. We use the 2MASS apparent K -band magnitude $K = 10.96$ (Saxton et al. 2017) and adopt the average mass-to-light ratio (M/L_K) as a function of total stellar mass from the appendix of Bell et al. (2003) to estimate the total stellar mass of the host of XMMSL1 J0740. Because the stellar mass-to-luminosity ratio M/L_K is color-based (although it is less sensitive in K -band) and we lack the color information, the total stellar mass of host galaxy is only a rough estimate. We notice that the BH mass of XMMSL1 J0740, $M_{\text{BH}} \sim 10^{7.05}M_{\odot}$, estimated from the total stellar mass is consistent with the results of Saxton et al. (2017). Because it is difficult to compute the uncertainties of the total stellar mass of host galaxy, the uncertainty of BH mass in Column 10 is only due to the scatter of the $M_{\text{BH}}-M_{\text{tot}}$ relation. Col. 11 give the ratio (B/T) of the bulge and total stellar mass of host galaxy. Because the bulges of host galaxies of most TDEs are not resolved, we estimate B/T from the empirical relation between the mass ratio B/T and the total stellar mass of galaxy (Stone et al. 2018). The correlation of the mass ratio B/T and the total stellar mass of galaxy has a very large scatters, for example, B/T of S0 galaxy can be as large as 0.7 and also as small as 0.1 (Gao et al. 2019). The total stellar masses of the sample galaxies in Gao et al. (2019) are binned and the ratio B/T in Table 1 is the average for each bin of the total stellar masses and have very large uncertainties.

In Table 1, Columns 12 and 13 give the peak bolometric luminosities and references, respectively. Ideally, the peak bolometric luminosities would be obtained by integrating the spectral energy distribution (SED) from the optical/UV to the X-ray waveband at the time of peak brightness. However, in practice, we can never observe the EUV (because of Galactic extinction). Therefore, an extrapolation from a single or several wavebands to obtain bolometric luminosity is always required. Different approaches have been followed in the literature: Some authors only measured the luminosity in the observed band without any further extrapolation. For an accretion disk of inner edge at the ISCO as an analogue of AGNs and black hole X-ray binaries, the disk emissions are broader than a single black body and some authors applied a bolometric correction of the kind we observe and apply in AGN, which can be up to a factor of 10 to account for an unobservable EUV bump. However, for an elliptical accretion disk, the accretion disk is truncated at an inner edge much larger than the ISCO, $a_{\text{in}} \simeq r_{\text{ms}}/(1-e_{\text{d}}) \sim r_{\text{ms}}a_{\text{mb}}/[(1-e_{\text{mb}})a_{\text{mb}}] \sim [r_{\text{ms}}/r_{\text{ISCO}}][a_{\text{mb}}/r_{\text{p}}]r_{\text{ISCO}} \sim 50\beta m_*^{-1/3} M_{\odot}^{1/3} r_{\text{ISCO}}$, the disk emissions at EUV and soft X-ray wavebands are expected to be much less significant than those of standard thin accretion disk. The observed SEDs of TDEs can be fitted well by a single black body and the emissions of standard thin accretion disk are much higher than the observational constraints of the spectroscopies and SEDs of TDEs (e.g. Gezari et al. 2012; Holoien et al. 2014, 2016b; Brown et al. 2017). Therefore, many authors approximated the observed SED by a single black body and then determined the bolometric luminosity by integrating over this single black body. In our paper, we follow the last method and calculate the bolometric luminosity by integrating over a single black body for the optical and UV radiation and adding the observations of soft X-ray wavebands at the time of peak brightness, except for the X-ray TDE XMMSL1 J0740. For XMMSL1 J0740, we used the bolometric luminosity in Saxton et al. (2017). The optical/UV fluxes of TDEs are corrected both for the Galactic extinction and starlights of host galaxy. No correction to the intrinsic dust extinction of host galaxies is made

because no evidence of significant internal dust extinction is reported for most TDEs in the literature. The optical emission line ratios between He II $\lambda = 3203$ and $\lambda = 4686$ suggests that the intrinsic dust extinction of the host galaxy might be important for the TDE PS1-10jh (Gezari et al. 2012). However, the origin of the broad optical emission lines remains unclear and is most probably either in the optically thick outflow envelopes (Roth et al. 2016) or the highly eccentric optically-thick accretion disk (Liu et al. 2017), and the ratio of optical emission lines may not be an implication of significant internal dust extinction of TDEs. For GALEX D23H-1, significant global extinction may be measured with the Balmer decrement of the H II region but the extinction in the line of sight to the flare may be different (Gezari et al. 2009). The optical luminosities for most optical/UV TDEs except TDE candidate SDSS J0952+2143 are the integral of the blackbody fit of the SED with the temperature obtained with multiple-waveband observations at the peak of light curve. In case that the measurement of temperature at peak is not available, it is extrapolated with the observations at time after peak with the assumption of constant temperature. For the TDE candidate SDSS J0952+2143, only the unfiltered observations are available at the time of peak brightness. We approximated the optical-UV SED with a black body of temperature 3.5×10^4 K (Komossa et al. 2008).

The X-ray luminosity at peak brightness of TDEs is included in the bolometric luminosity, when it is available. The X-ray radiation at the time of peak brightness is either not detected or insignificant for most of the optical/UV TDEs of the sample sources except for ASASSN-14li. Significant X-ray radiation is detected at peak for ASASSN-14li (Brown et al. 2017). The optically selected TDE candidate GALEX D1-9 was detected in X-ray after about 2.1 years after peak (Gezari et al. 2008). It is unclear if the source at peak was bright in X-ray because no observation was made in X-ray. Significant X-ray radiation has been detected at the late time after discovery for the optical TDEs ASASSN-15oi (Gezari et al. 2017), PTF09axc, PTF09ge, and ASASSN-14ae (Jonker et al. 2019). However, the observations of these TDE sources at the time of peak showed that they are extremely weak in X-ray. Therefore, it is possible that the optical TDE GALEX D1-9 is also weak in X-ray at peak. The peak bolometric luminosity of GALEX D1-9 in Table 1 is the integral of the blackbody fit of the optical/UV SED at peak. Because it is difficult to estimate the uncertainties of the peak bolometric luminosities, we arbitrarily assign an uncertainty of 0.2-dex (or about 60%) to each of the peak bolometric luminosity.

Columns 14 and 15 of Table 1 give the total radiation energies after peak and the associated references. When the total radiation energy after peak in the literature is integrated up only to the end of observational campaign, we calculate the total radiation energy ΔE by extrapolating the observations to infinity of time with equation (16) except for ASASSN-14ae and PS18kh, and have

$$\Delta E = \frac{\Delta E_0}{1 - [L_e/L_p]^{1-1/n}} \quad (25)$$

with $n = 5/3$, where ΔE_0 given in the literature is the radiation energy integrated from the peak time t_p to the time t_0 of the end of the observational campaign and L_e is the luminosity at t_0 . For ASASSN-14ae, an exponential decay is adopted because the bolometric luminosity is best fitted with an exponential (Holoien et al. 2014). PS18kh re-brightens at about 50 days (rest-frame) after peak until 70 days after peak when the observational campaign ends. We extrapolate the observations by assuming a power-law decay of the luminosity given by Equation (16) and taking t_d from Holoien et al. (2019a). It is difficult to estimate the uncertainties of the total radiation energy. We arbitrarily assign a 0.2-dex uncertainty to the total radiation energy for simplicity.

4.2. Consistency of the expectations and observations

Figure 2 gives the observations of the peak bolometric luminosity and the total radiation energy together with the associated 0.2-dex uncertainties of the sample sources as a function of the BH mass calculated with the $M_{\text{BH}} - \sigma_*$ relation. Because the observational errors of the peak bolometric luminosity and the total radiation energy after peak of nearly all the sample sources of TDEs are not given in the literature, we arbitrarily assigned a 0.2-dex (or about 60%) uncertainties to each of the observations to include the observational errors, the short-time scale variations, and the possibly missed radiation in Infrared and extreme UV wavebands. Figure 2 shows that the observations of the peak bolometric luminosity and the total radiation energy are consistent with the expectations of the elliptical accretion disk model with orbital penetration factor $\beta = 1$, but much smaller than those expected with the canonical radiation efficiency $\eta = 0.1$. The results suggest that the sample TDE source except SDSS J0952+2143 probably result from the tidal disruptions of A-type or later stars by SMBHs of mass between $10^5 M_\odot$ to $10^7 M_\odot$. The disrupted star of SDSS J0952+2143 is probably an early A-type or late B-type star. This is consistent with the observations that the host galaxies of most TDEs except SDSS J0952+2143 are post-starbursts with bursts of star formation about gig-years ago and are deficient of B- and O-type stars but in rich of A- and later-type stars (Arcavi et al. 2014; French et al. 2016; Graur et al. 2018; Law-Smith et al. 2017). The observations of host galaxy of TDE SDSS J0952+2143 is a star-forming galaxy in rich of early B- or O-type stars (Palaversa et al. 2016) and consistent with the spectral type of the disrupted star.

Figure 2 shows that the observations of the peak bolometric luminosity L_p and the total radiation energy after peak ΔE are generally consistent with the expectations of the elliptical accretion disk but locate in different regions of stellar mass. Equations (19) and (21) suggest that both the peak bolometric luminosity and the total radiation energy after peak depend on both the masses of star and BH and the orbital penetration factor β . Provided the BH mass M_{BH} with the $M_{\text{BH}} - \sigma_*$ relation, L_p and ΔE depend on both the mass M_* and the orbital penetration factor β of star and the inconsistency of stellar masses required by L_p and ΔE in Figure 2 is probably because the penetration factor β of TDEs may not be exactly unit. Provided L_p , ΔE , and M_{BH} , we can solve the equations (19) and (21) to obtain the mass M_* and orbital penetration factor β .

4.3. Mass of star and accreted fraction

With the observations of the BH mass M_{BH} , the peak bolometric luminosity L_p , and the total radiation energy after peak ΔE (or apparent accreted stellar mass ΔM_{app}), we can solve the equations (19) and (21) (or (22)) to obtain the mass and orbital penetration factor of star. We solve the equations with the method of Monte Carlo Markov Chain (MCMC) using *python* package *emcee* (Foreman-Mackey et al. 2013), together with the likelihood function

$$-\frac{1}{2} \left[\frac{(\lg L_p - \lg L'_p)^2}{\sigma_L^2} + \ln(2\pi\sigma_L^2) + \frac{(\lg \Delta E - \lg \Delta E')^2}{\sigma_E^2} + \ln(2\pi\sigma_E^2) \right], \quad (26)$$

where L_p and ΔE are, respectively, the observations of the peak bolometric luminosity and the total radiation energy after peak, L'_p and $\Delta E'$ are, respectively, the estimates of equations (19) and (21) with the input parameters (M_{BH} , M_* , and β), σ_L of 0.2-dex is the uncertainty of the peak bolometric luminosity, and σ_E of 0.2-dex is the uncertainty of the total radiation energy after peak. The prior parameters of the MCMC experiments are the BH mass M_{BH} , the stellar mass M_* , and the orbital penetration factor β of star. The prior distribution of M_* and β are uniform in the ranges of $0.01 M_\odot < M_* < 150 M_\odot$ and $0.9 < \beta < 2.5$, respectively. The lower limit $\beta = 0.9$ is adopted to be about the lower limit of full disruptions of low mass stars, while the upper limit $\beta = 2.5$ is due to the limitation of the hydrodynamic simulations (Guillochon &

Ramirez-Ruiz 2013). Because both the peak bolometric luminosity L_p and the total radiation energy after peak ΔE depend on the penetration factor β mostly because of the radiation efficiency η , the solutions of equations (19) and (21) would give poor constraints of the penetration factor and are nearly insensitively to the values of the upper and lower limits of β , except that no solution can be found within the range. The prior distribution of the parameter M_{BH} is given with a normal distribution whose mean and variance are, respectively, the observation and uncertainties given in Column 7 of Table 1. The MCMC chain includes 100 walkers with each walker consisting of 10^4 steps. The first 50% of the steps of each walker are removed for burn-in and one set of the parameters is saved every 5 steps for the rest of walker. For each walker, the parameters begin with the local best-fit results from the least-squared method plus a small random offset.

Figure 3 gives the posterior distributions of model parameters (M_{BH} , M_* , and β) of the MCMC experiments and Table 2 gives the results of the parameters M_* and β and the associated uncertainties at the 90-percent confidence level obtained with the MCMC method. Figure 3 shows that the BH and stellar masses of TDEs can be well determined but the orbital penetration factor of star is constrained poorly, which are consistent with the arguments for TDEs with $\Delta = 0.25\beta^3 r_*^{-2} m_*^{1/3} M_6^{5/3} \lesssim 1$, or with $\beta \sim 1$ and $M_{\text{BH}} \lesssim 10^{6.5} M_\odot$ given at the end of Sec.3. Our MCMC experiments show that some TDEs may have two solutions, one associated with main sequence star and the other associated with brown dwarf. It is possible because the main-sequence stars and brown dwarfs have significantly different relations of stellar mass and radius with dramatical change from $M_* \sim 0.07$ to $0.08 M_\odot$: The radius increases with mass for main sequence stars but decreases with mass for brown dwarf. We do not simply remove the solutions associated with the brown dwarfs. We compare the probabilities of the posterior distributions of the two solutions and adopt the one with higher posterior probability to be the main solution of TDE. Figure 3 gives the posterior distributions of the model parameters of the main solution. We give our conclusions based on the primary solutions of the TDEs. However, when the two solutions have comparable probabilities of the posterior distributions with the ratio of probability less than 3 : 1, we keep both solutions and give the secondary solution in the row of Table 2 after the primary.

Figure 4 gives the masses of stars of the 11 TDEs obtained with the MCMC experiments, including both the primary and secondary possible solutions of the stellar masses. Figure 4 and Table 2 shows that the stars have spectral types in the range of from A- through M-type main sequence stars to brown dwarfs. Among all the eleven sample sources with BH mass obtained with $M_{\text{BH}}-\sigma_*$ relations, iPTF16fnl and GALEX D23H-1 have two solutions with the primary solution associated with brown dwarf and the secondary associated with main sequence star. The TDE iPTF16fnl has the lowest total radiation energy and the second lowest peak bolometric luminosities after GALEX D23H-1. The spectral observations of the host galaxy show that iPTF16fnl with light curves of decay timescales among the shortest is the nearest of the TDEs discussed in our paper and has a BH of lowest mass at center (Blagorodnova et al. 2017; Onori et al. 2019). Therefore, the main solution of iPTF16fnl associated with brown dwarf is most probably the actual solution of the source. TDE GALEX D23H-1 has the lowest peak bolometric luminosity and is one of the sources with the lowest total radiation energy, leading to the solution of brown dwarf. However, the low peak bolometric luminosity and total radiation energy of GALEX D23H-1 might not be intrinsic but rather due to the possible intrinsic dust extinction of host galaxy, because a global extinction may have been measured with the Balmer decrement of the H II regions and the extinction in the line of sight to the flare might be important (Gezari et al. 2009). Except iPTF16fnl and GALEX D23H-1, the other 9 sample sources with observations of BH mass have solutions associated with late-type main sequence stars. The observations that the stars of the TDE sources are late-type main sequences or brown dwarfs are well consistent with the observations of host

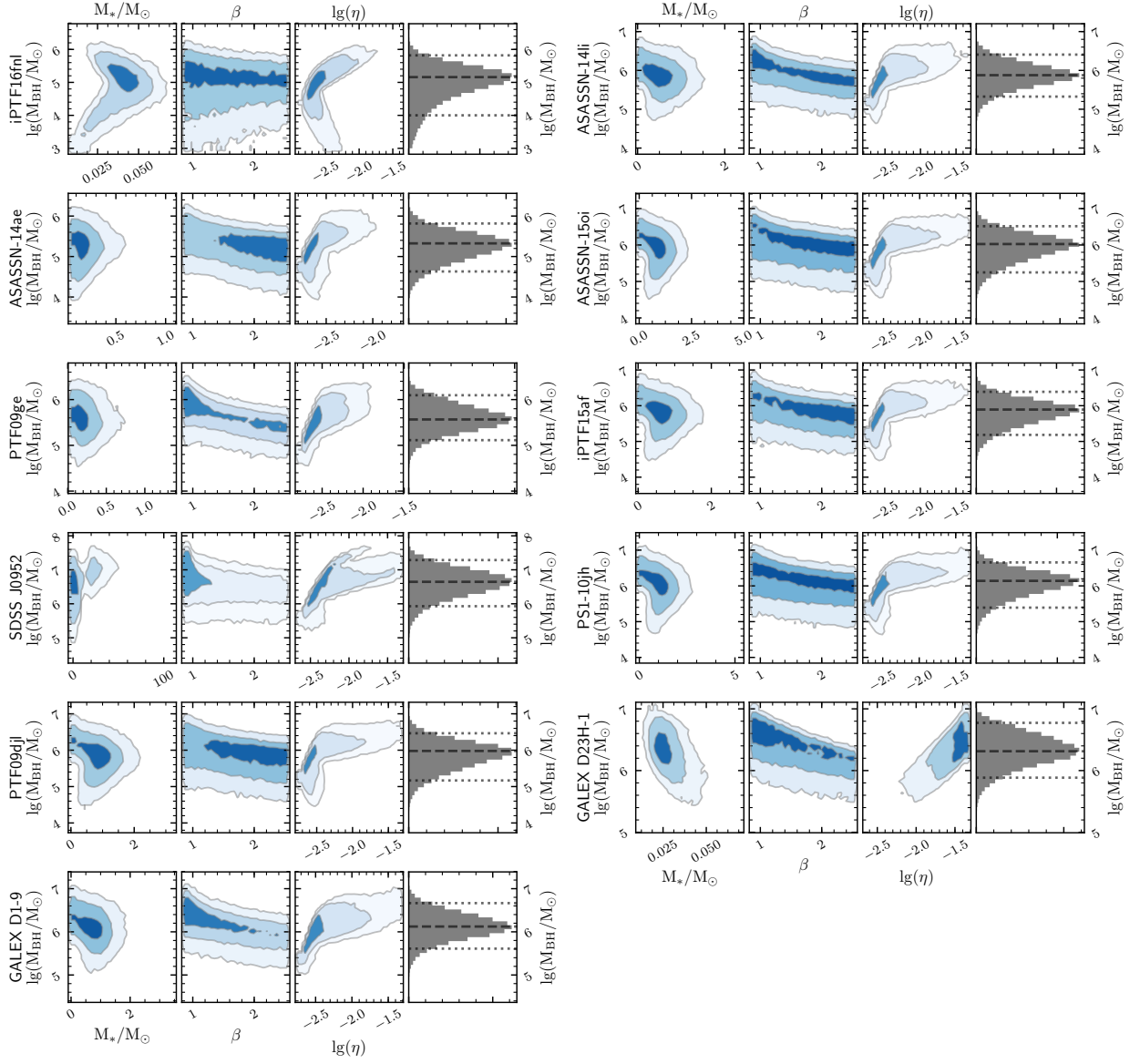


Figure 3. Posterior distributions of model parameters (M_{BH} , M_* , and β) and radiation efficiency (η) of the MCMC experiments. The prior distribution of M_{BH} is given with a normal distribution whose mean and variance are, respectively, the observation and uncertainties given with the $M_{\text{BH}} - \sigma_*$ relation. The contours are for 1, 2, and 3 σ . In the histogram of M_{BH} , dashed line indicate the BH mass at the peak of distributions and two dotted lines give the BH mass ranges at the 90-percent confidence level.

galaxies that the host galaxies of most TDEs except SDSS J0952+2143 are post-merger E+A galaxies with bursts of star formation about gig-years ago and are dominated with A-type stars and later (Arcavi et al. 2014; French et al. 2016, 2017).

When we calculate the peak bolometric luminosity with $L_p = \eta \dot{M}_p c^2$ and the total radiation energy $\Delta E = \eta \Delta M_* c^2$ with the radiation efficiency η given by Equation (9), we have implicitly assumed that the peak bolometric luminosity is sub-Eddington. However, when the peak fallback rate \dot{M}_p is near or above the Eddington accretion rate $\dot{M}_{\text{Edd}} = L_{\text{Edd}}/(\eta c^2)$, the peak luminosity L_p scales as (Paczynski 1980) $L_p \simeq L_{\text{Edd}} [1 + \lg(\dot{M}_p/\dot{M}_{\text{Edd}})]$ because of the photon trapping and a significant fraction of radiation being

advected onto the BH (Abramowicz et al. 1988). For TDEs with $\dot{M}_p \lesssim \dot{M}_{\text{Edd}}$, the peak luminosity and the light curve of TDEs are capped with the Eddington luminosity. To compare the observations of TDEs with the predictions of elliptical accretion disk model, we excluded the TDE candidates from the sample TDE sources with a significant extended period of flat peak luminosity (most TDE candidates are in AGNs). At the mean time, the transient surveys of TDEs have more priority to detect brighter sources. It is expected to preferentially detect TDEs with peak luminosity at or near Eddington luminosity. For $L_p \sim L_{\text{Edd}}$, Equation (19) gives

$$m_* \simeq \left(\frac{1.25}{1.78}\right)^{6/(5+9\zeta)} \left[\left(\frac{\eta_0}{0.059}\right) \left(\frac{A_\gamma}{1.328}\right)^{-1} \beta (1+\Delta)^{-1} \right]^{6/(5+9\zeta)} \left(\frac{L_p}{L_{\text{Edd}}}\right)^{6/(5+9\zeta)} M_6^{11/(5+9\zeta)} \\ \simeq 0.70^{6/(5+9\zeta)} \left(\frac{L_p}{L_{\text{Edd}}}\right)^{6/(5+9\zeta)} M_6^{11/(5+9\zeta)}. \quad (27)$$

For $\zeta \simeq 0.21$, we have

$$m_* \simeq 0.70^{6/6.89} \left(\frac{L_p}{L_{\text{Edd}}}\right)^{6/6.89} M_6^{11/6.89}. \quad (28)$$

Figure 4 overplots the selection effects of Equation (28) for $L_p = L_{\text{Edd}}$ and $L_p = 0.1L_{\text{Edd}}$. Taking into account of the large intrinsic scatter of the $M_{\text{BH}} - \sigma_*$ relation ($\sigma = 0.49$ dex or $3\sigma = 1.47$ dex), Figure 4 shows that the masses of star may correlate with the masses of BHs, consistent with the suggestion of Equation (28).

Provided M_{BH} , M_* , and β , we can calculate the radiation efficiency of TDEs, $\eta = \eta(M_{\text{BH}}, R_*, M_*, \beta)$, with equation (9) and the MCMC method. The posterior distributions of the radiation efficiency (η) of the MCMC experiments are given in Figure 3 and the radiation efficiencies and associated uncertainties at the 90-percent confidence level obtained with the MCMC method are given in Table 2. Figure 1 shows the radiation efficiencies and associated uncertainties at the 90-percent confidence level as a function of BH mass. The BH masses of TDEs are computed with the $M_{\text{BH}} - \sigma_*$ relation of host galaxies and stellar velocity dispersions in Table 1. Figure 1 shows that the radiation efficiencies of all the TDEs are much less than the canonical value $\eta = 0.1$ popularly adopted for TDEs in the literature. All the TDE sources except GALEX D23H-1 have a typical radiation efficiency $\lg(\eta) \simeq -2.57$ or $\eta \simeq 2.7 \times 10^{-3}$, which is about 37 times smaller than the canonical radiation efficiency. A low radiation efficiency would lead to a low peak bolometric luminosity and total radiation energy with provided accretion rate of matter. Or, provided the observations of the peak bolometric luminosity and the total radiation energy after peak, we should obtain a much higher apparent accretion rate and total accreted stellar material with the low radiation efficiency than what obtained with the canonical radiation efficiency in the literature. It suggests that the low bolometric peak luminosity and total radiation energy of TDEs would result from the low conversion efficiency of matter into radiation of elliptical accretion disk.

Table 2 and Figure 5 give the mass of accreted material ΔM_* and its ratio to the mass of star (or the accreted fraction of stellar mass) $\Delta M_*/M_*$ used in the MCMC experiments. The accreted stellar mass together with the conversion efficiency give the expected total radiation energy $\Delta E' = \eta \Delta M_* c^2$ of Equation (26). In Table 2 and Figure 5, we also give the associated uncertainties of ΔM_* and $\Delta M_*/M_*$ at the 90-percent confidence level obtained with the MCMC experiments. Equation (20) shows that the relative accreted stellar mass can be obtained with $\Delta M_*/M_* \simeq (1-n)^{-1} A_\gamma B_\gamma \simeq 1.5 A_\gamma B_\gamma$, which depends on the stellar structure and orbital penetration factor β (Lodato et al. 2009; Guillochon & Ramirez-Ruiz 2013; Golightly et al. 2019; Law-Smith et al. 2019; Ryu et al. 2019). In Figure 5, we also give the $\Delta M_*/M_*$ for both $\gamma = 5/3$

Table 2. Results of the MCMC experiments for the TDEs with BH mass provided.

Name	M_* (M_\odot)	β	$\lg(\eta)$	ΔM_* (M_\odot)	$\Delta M_*/M_*$
(1)	(2)	(3)	(4)	(5)	(6)
iPTF16fnl ^a	0.040 ^{+0.015} _{-0.017} 0.081 ^{+0.054} _{-0.008}	0.9 ^{+1.4} _{-0.0} 2.5 ^{+0.0} _{-1.3}	-2.68 ^{+0.45} _{-0.12} -2.74 ^{+0.18} _{-0.04}	0.012 ^{+0.005} _{-0.005} 0.026 ^{+0.011} _{-0.008}	0.34 ^{+0.00} _{-0.09} 0.34 ^{+0.00} _{-0.10}
ASASSN-14li	0.46 ^{+0.49} _{-0.38}	0.9 ^{+1.4} _{-0.0}	-2.57 ^{+0.54} _{-0.14}	0.15 ^{+0.13} _{-0.13}	0.34 ^{+0.00} _{-0.09}
ASASSN-14ae	0.14 ^{+0.17} _{-0.07}	2.5 ^{+0.0} _{-1.4}	-2.69 ^{+0.30} _{-0.06}	0.043 ^{+0.047} _{-0.022}	0.34 ^{+0.00} _{-0.09}
ASASSN-15oi	0.88 ^{+0.56} _{-0.79}	0.9 ^{+1.4} _{-0.0}	-2.61 ^{+0.65} _{-0.09}	0.25 ^{+0.17} _{-0.23}	0.34 ^{+0.00} _{-0.09}
PTF09ge	0.16 ^{+0.21} _{-0.08}	0.9 ^{+1.4} _{-0.0}	-2.59 ^{+0.35} _{-0.14}	0.050 ^{+0.060} _{-0.028}	0.34 ^{+0.00} _{-0.09}
iPTF15af	0.66 ^{+0.42} _{-0.57}	2.4 ^{+0.0} _{-1.4}	-2.62 ^{+0.56} _{-0.08}	0.17 ^{+0.14} _{-0.15}	0.34 ^{+0.00} _{-0.09}
SDSS J0952+2143	3.03 ^{+21.55} _{-2.35}	0.9 ^{+1.3} _{-0.0}	-2.30 ^{+0.53} _{-0.28}	0.98 ^{+0.71} _{-0.76}	0.31 ^{+0.01} _{-0.28}
PS1-10jh	1.02 ^{+0.69} _{-0.89}	0.9 ^{+1.4} _{-0.0}	-2.55 ^{+0.68} _{-0.13}	0.32 ^{+0.18} _{-0.29}	0.34 ^{+0.00} _{-0.09}
PTF09djl	0.83 ^{+0.53} _{-0.74}	2.4 ^{+0.1} _{-1.4}	-2.61 ^{+0.58} _{-0.10}	0.24 ^{+0.15} _{-0.21}	0.34 ^{+0.00} _{-0.09}
GALEX D23H-1 ^a	0.025 ^{+0.012} _{-0.007} 0.13 ^{+0.21} _{-0.05}	0.9 ^{+1.4} _{-0.0} 0.9 ^{+1.3} _{-0.0}	-1.40 ^{+0.04} _{-0.41} -2.57 ^{+0.37} _{-0.13}	0.0075 ^{+0.0039} _{-0.0025} 0.042 ^{+0.059} _{-0.020}	0.34 ^{+0.00} _{-0.09} 0.34 ^{+0.00} _{-0.08}
GALEX D1-9	0.74 ^{+0.44} _{-0.66}	0.9 ^{+1.4} _{-0.0}	-2.54 ^{+0.68} _{-0.14}	0.23 ^{+0.13} _{-0.20}	0.34 ^{+0.00} _{-0.09}

^aThe source has two possible solutions and the main one with higher probability is given at the first entry.

NOTE—The BH masses are calculated with the $M_{\text{BH}} - \sigma_*$ relation. The uncertainties of model parameters are at the 90-percent confidence level obtained with MCMC experiments.

and $4/3$, and $\beta = 1$ calculated with the empirical formulae of A_γ and B_γ in the Appendix of [Guillochon & Ramirez-Ruiz \(2013\)](#). Figure 5 shows that the total accreted material after peak of TDEs significantly varies from about $10^{-2}M_\odot$ of GALEX D23H-1 and iPTF16fnl to about $1M_\odot$ of SDSS J0952+2143 but the relative accreted material to the total mass of star of TDEs except SDSS J0952+2143 is relatively constant with $\Delta M_*/M_* \sim 0.34$, which is given by the hydrodynamic simulations of tidal disruption of low mass star with polytropic index $\gamma = 5/3$. For SDSS J0952+2143, the star has a mass of about $3.03M_\odot$ and is described with the hybrid model. The relative accreted stellar mass of SDSS J0952+2143 is close to the expectation of the polytropic model $\gamma = 5/3$ but with very large uncertainties.

5. WEIGHING BLACK HOLES USING TDES

5.1. Deriving the BH and stellar masses with L_p and ΔE

It is essential to have an alternative to the $M_{\text{BH}} - \sigma_*$ relation to calculate the masses of BHs, when a BH is a member of a supermassive BH binary, or has an off-nuclear position, or in globular cluster. Equation (17) and (20) show that provided both the peak accretion rate \dot{M}_p and the total accreted material ΔM_* , one could uniquely determine the masses of BH and star by solving the equations. However, we cannot directly measured \dot{M}_p and ΔM_* but the peak bolometric luminosity L_p and the total radiation energy ΔE , which

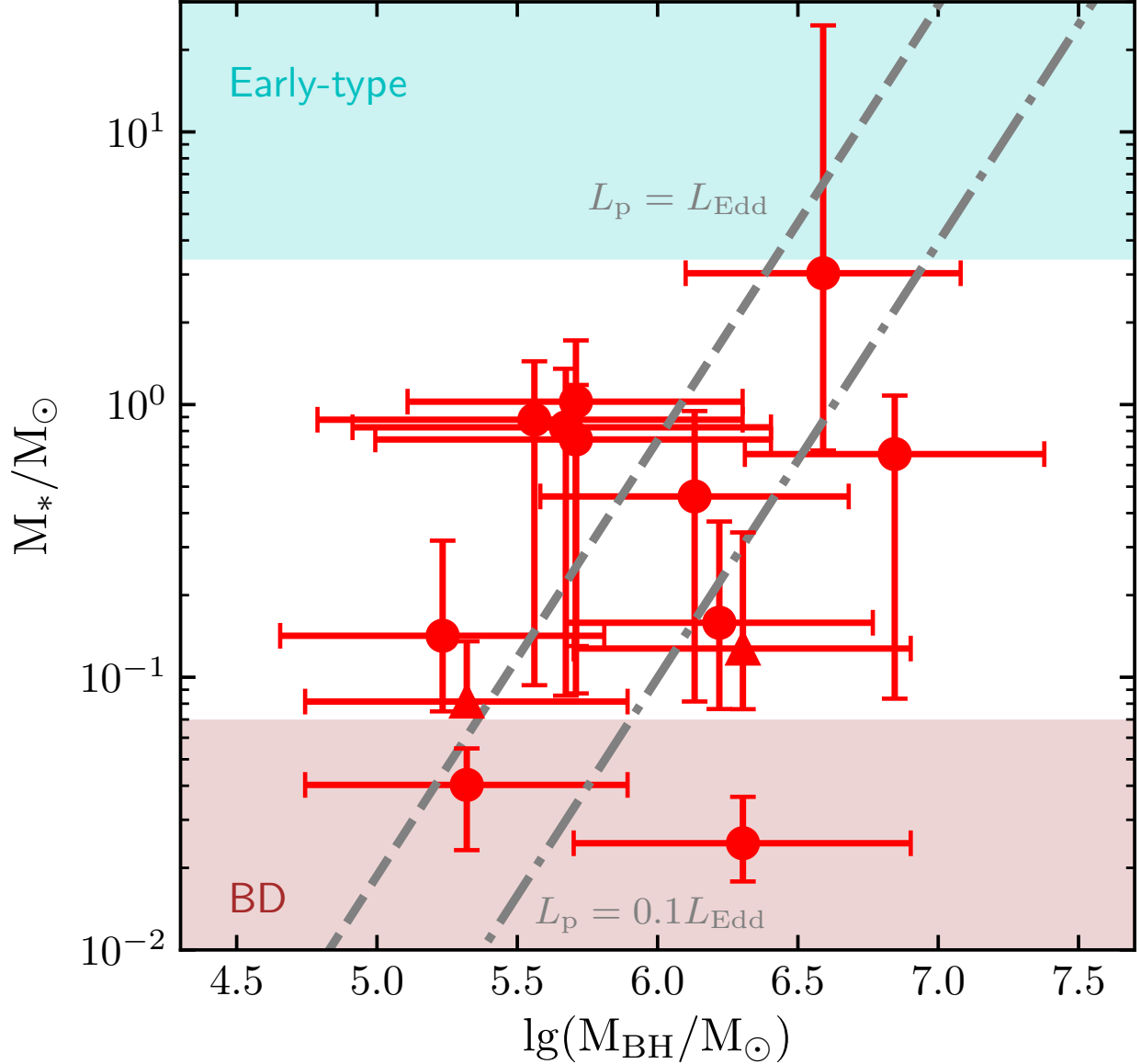


Figure 4. The stellar mass M_* (filled circle) of the sample sources vs BH mass. Filled triangle is for the secondary solutions of iPTF16fnl and GALEXD23H-1. The mass of star and associated uncertainty at 90% confidence level are calculated with MCMC methods and provided BH mass. The stars of the sample TDE sources are late-type main-sequences, consistent with the observations that the host galaxies of most TDEs are E+A post-starburst galaxies. The dashed and dash-dotted lines are, respectively, the observational selection effects of Equation (28) for $L_p = L_{\text{Edd}}$ and $0.1 L_{\text{Edd}}$ (see Sec. 4.3 for detailed discussions).

depends not only the masses of BH and star but also on the radiation efficiency and thus also on the the orbital penetration factor β . The masses of BH and star become functions of the penetration factor and would be expected to be determined observationally with larger uncertainties. Figure 3 shows that, provided the measurement of BH mass with the $M_{\text{BH}}-\sigma_*$ relation, the orbital penetration factor β cannot be well constrained with very large uncertainties of nearly the entire range of sampling $0.9 < \beta < 2.5$ for most TDEs. The large uncertainties of the measurements of β are consistent with the arguments and conclusions of Sec. 3 that the peak luminosity and total radiation energy of TDEs are nearly independent of the penetration

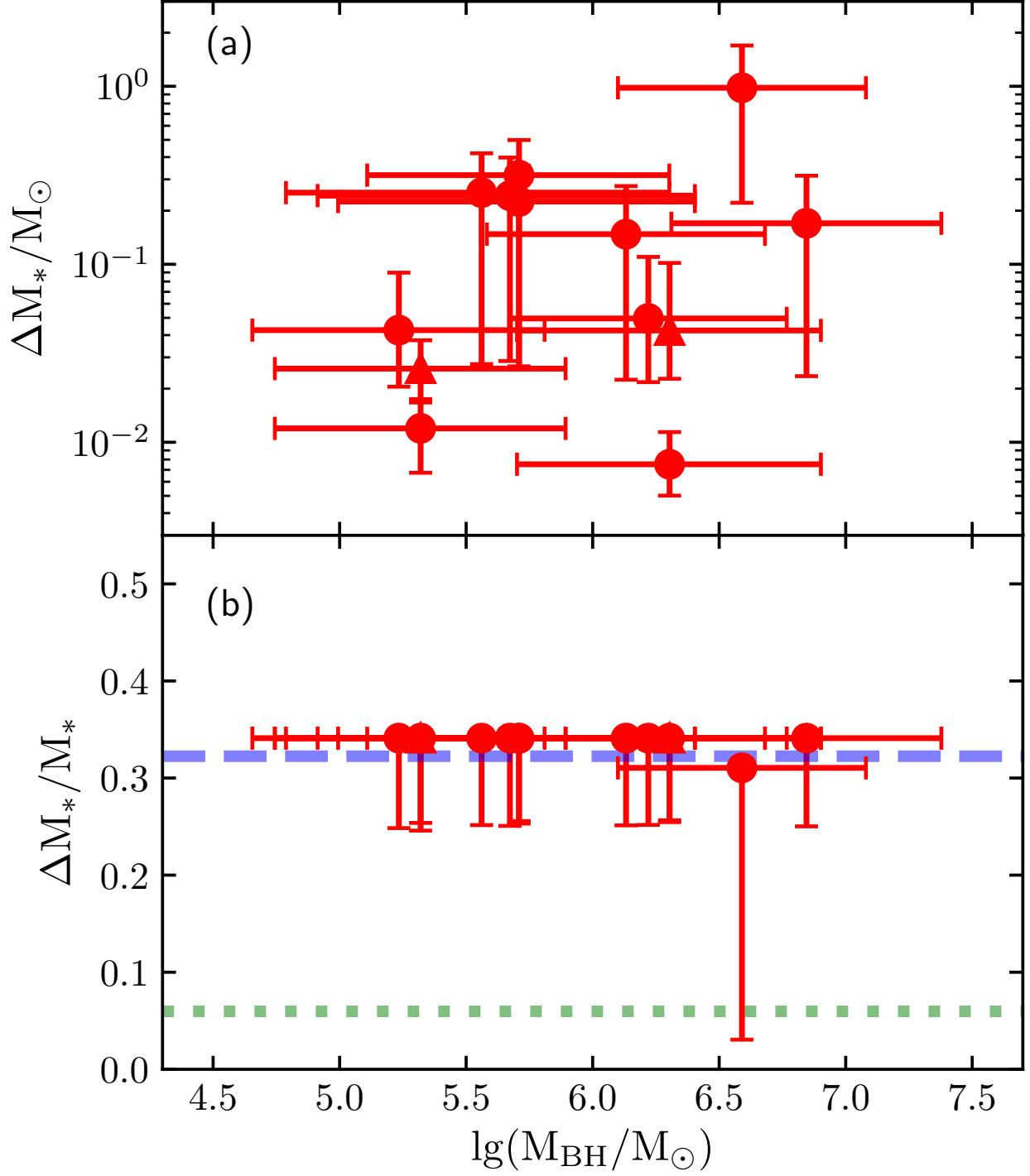


Figure 5. Accreted stellar mass after peak (*upper*) and the relative accreted fraction (*lower*) vs BH mass of the sample sources in Table 2. *Lower*: Dashed and dotted lines give, respectively, the expectations with the polytropic model $\gamma = 5/3$ for low mass stars and $\gamma = 4/3$ for high mass stars for $\beta = 1$. The result of SDSS J0952+2143 with $M_* \simeq 3M_{\odot}$ is obtained with the hybrid polytropic model and close to the expectation with the polytropic model $\gamma = 5/3$.

factor for the range $0.7 \lesssim \beta \lesssim 2.1$ and implies that the masses of BH do not significantly couple with the penetration factor. Therefore, we expect to determine the masses of BH and star with fairly small uncertainties by solving the equations (19) and (21) with the observations of L_p and ΔE . An unrestraint penetration factor would not lead to significant increases of the uncertainties of the measurements of the masses of BHs and stars.

With the observations of L_p and ΔE , we solve the equations with the MCMC method as described in Sec. 4.3, except that the prior distributions of all the three parameters M_{BH} , M_* and β are now uniform in the ranges $10^3 M_\odot \leq M_{\text{BH}} \leq 10^9 M_\odot$, $0.01 M_\odot < M_* < 150 M_\odot$, and $0.9 \leq \beta \leq 2.5$. The large ranges of masses of BHs and stars require a large amount of computation costs. In order to enhance convergence rate of MCMC experiments and alleviate the burden of computations, we start the MCMC experiments with $\beta = 1$ and the masses of BH and star obtained by solving the equations (19) and (21) for $\beta = 1$ and the observations of L_p and ΔE . We adopted $\beta = 1$ and the solutions of equations (19) and (21) for $\beta = 1$ as the initials of the parameters of the MCMC walkers, because TDEs are expected to happen predominantly at $\beta \sim 1$ (Stone & Metzger 2016; Kochanek 2016). Because the results of the masses of BHs and stars of TDEs depends only weakly on the penetration factor, in fact the solutions for $\beta = 1$ are good approximations of the results.

We solve the equations for all the TDEs in Table 1 and give the posterior distributions of the model parameters ($\lg M_{\text{BH}}$, M_* , and β) of the MCMC experiments in Figure 6 and Figure 7 for TDEs with and without the observations of stellar velocity dispersion of host galaxies, respectively. In Figure 6 and Figure 7, we also give the posterior distributions of the associated radiation efficiency $\lg \eta$ of the MCMC experiments. When a TDE has two possible solutions with comparable posterior probabilities, we give the posterior distributions for the primary solution in Figure 6. Table 3 give the results of the masses of BH and star, the radiation efficiency, and the associated uncertainties at the 90-percent confidence level obtained with the MCMC experiments. The TDE sources in Table 3 are listed with the same order as in Table 1. The posterior distributions of the model parameters (M_{BH} , M_* , β , and η) of the MCMC experiments in Figure 6 are closely similar to those in Figure 3, implying that L_p and ΔE only can determine the mass of star, penetration factor, and radiation efficiency as well as when the BH masses are provided. In Figure 8, we compare the masses of stars obtained with L_p and ΔE but without the knowledge of BH mass and those determined with L_p and ΔE together with the BH masses calculated with the $M_{\text{BH}}-\sigma_*$ relation. Figure 8 shows that the stellar masses are consistent with each other. Our results suggest that the mass of star of TDEs and the accreted matter can be well determined with the peak bolometric luminosity L_p and the total radiation energy ΔE only. Figure 9 gives the mass of star of all the TDE sample sources obtained with L_p and ΔE . Figure 9 shows that the distribution of the spectral types of star of the TDEs without observation of stellar velocity dispersions of host galaxy is consistent with that of the TDEs with the observations of stellar velocity dispersions and the stars of the TDE sample sources except iPTF16fnl and GALEX D23H-1 are A- or later-type main-sequence stars, which are consistent with the conclusions obtained only with TDEs with the observations of stellar velocity dispersions of host galaxies. Figure 9 shows that the X-ray TDE XMMSL1 J0740 has the largest stellar mass for a given black hole mass. However, the difference is not significant and TDE XMMSL1 J0740 is the only sample source discovered in the X-ray wavebands. Much more sample sources of X-ray discovery TDEs are needed. The correlation of masses of star and BH may due to the observational selection effects, as suggested by equation (28).

In Figure 10(a), we compare the BH masses of TDEs in Table 3 obtained with L_p and ΔE to those in Table 1 calculated with the $M_{\text{BH}}-\sigma_*$ relation. The one-to-one line and the intrinsic scatters of the $M_{\text{BH}}-\sigma_*$ relations are given to show the expected correlation and intrinsic scatters of the BH masses obtained

Table 3. Results of the MCMC experiments for all the sample sources.

Name	$\lg(M_{\text{BH}})$ (M_{\odot})	M_* (M_{\odot})	β	$\lg(\eta)$	ΔM_* (M_{\odot})	$\Delta M_*/M_*$
(1)	(2)	(3)	(4)	(5)	(6)	(7)
iPTF16fnl ^a	5.16 ^{+0.66} _{-1.16}	0.040 ^{+0.015} _{-0.017}	0.9 ^{+1.4} _{-0.0}	-2.68 ^{+0.43} _{-0.13}	0.012 ^{+0.005} _{-0.005}	0.34 ^{+0.00} _{-0.09}
	4.96 ^{+0.51} _{-0.45}	0.082 ^{+0.055} _{-0.008}	2.5 ^{+0.0} _{-1.3}	-2.73 ^{+0.17} _{-0.05}	0.025 ^{+0.013} _{-0.007}	0.34 ^{+0.00} _{-0.10}
ASASSN-14li	5.88 ^{+0.53} _{-0.55}	0.41 ^{+0.53} _{-0.33}	0.9 ^{+1.4} _{-0.0}	-2.56 ^{+0.53} _{-0.14}	0.14 ^{+0.13} _{-0.12}	0.34 ^{+0.00} _{-0.09}
ASASSN-14ae	5.32 ^{+0.49} _{-0.69}	0.14 ^{+0.18} _{-0.06}	2.5 ^{+0.0} _{-1.4}	-2.69 ^{+0.31} _{-0.06}	0.043 ^{+0.047} _{-0.022}	0.34 ^{+0.00} _{-0.09}
ASASSN-15oi	6.03 ^{+0.49} _{-0.78}	0.89 ^{+0.53} _{-0.81}	2.3 ^{+0.1} _{-1.3}	-2.59 ^{+0.63} _{-0.10}	0.26 ^{+0.16} _{-0.23}	0.34 ^{+0.00} _{-0.09}
PTF09ge	5.57 ^{+0.53} _{-0.45}	0.15 ^{+0.22} _{-0.07}	0.9 ^{+1.4} _{-0.0}	-2.59 ^{+0.35} _{-0.14}	0.048 ^{+0.060} _{-0.026}	0.34 ^{+0.00} _{-0.09}
iPTF15af	5.89 ^{+0.50} _{-0.71}	0.57 ^{+0.51} _{-0.48}	2.5 ^{+0.0} _{-1.4}	-2.62 ^{+0.57} _{-0.08}	0.17 ^{+0.15} _{-0.14}	0.34 ^{+0.00} _{-0.09}
SDSS J0952+2143	6.65 ^{+0.64} _{-0.72}	2.99 ^{+21.11} _{-2.35}	0.9 ^{+1.3} _{-0.0}	-2.31 ^{+0.54} _{-0.27}	0.97 ^{+0.72} _{-0.75}	0.31 ^{+0.01} _{-0.28}
PS1-10jh	6.14 ^{+0.52} _{-0.75}	1.05 ^{+0.64} _{-0.95}	0.9 ^{+1.4} _{-0.0}	-2.57 ^{+0.70} _{-0.12}	0.30 ^{+0.20} _{-0.27}	0.34 ^{+0.00} _{-0.09}
PTF09djl	5.98 ^{+0.49} _{-0.81}	0.80 ^{+0.55} _{-0.71}	2.3 ^{+0.1} _{-1.3}	-2.61 ^{+0.61} _{-0.09}	0.24 ^{+0.16} _{-0.21}	0.34 ^{+0.00} _{-0.09}
GALEX D23H-1 ^a	6.31 ^{+0.46} _{-0.43}	0.025 ^{+0.012} _{-0.007}	0.9 ^{+1.4} _{-0.0}	-1.40 ^{+0.03} _{-0.43}	0.0074 ^{+0.0040} _{-0.0023}	0.34 ^{+0.00} _{-0.09}
	5.64 ^{+0.55} _{-0.40}	0.12 ^{+0.22} _{-0.05}	0.9 ^{+1.3} _{-0.0}	-2.58 ^{+0.38} _{-0.13}	0.047 ^{+0.057} _{-0.024}	0.34 ^{+0.00} _{-0.08}
GALEX D1-9	6.12 ^{+0.54} _{-0.51}	0.71 ^{+0.47} _{-0.63}	0.9 ^{+1.4} _{-0.0}	-2.54 ^{+0.69} _{-0.14}	0.20 ^{+0.15} _{-0.18}	0.34 ^{+0.00} _{-0.09}
XMMSL1 J0740	5.63 ^{+0.52} _{-0.91}	0.42 ^{+0.52} _{-0.32}	2.5 ^{+0.0} _{-1.4}	-2.65 ^{+0.34} _{-0.07}	0.13 ^{+0.14} _{-0.09}	0.34 ^{+0.00} _{-0.09}
AT2018dyb	5.82 ^{+0.51} _{-0.69}	0.46 ^{+0.47} _{-0.38}	2.4 ^{+0.1} _{-1.4}	-2.64 ^{+0.53} _{-0.07}	0.14 ^{+0.12} _{-0.12}	0.34 ^{+0.00} _{-0.09}
ASASSN-19bt	5.88 ^{+0.52} _{-0.65}	0.53 ^{+0.51} _{-0.44}	0.9 ^{+1.4} _{-0.0}	-2.59 ^{+0.54} _{-0.12}	0.16 ^{+0.14} _{-0.14}	0.34 ^{+0.00} _{-0.09}
AT2018fyk	6.27 ^{+0.52} _{-0.79}	1.39 ^{+0.88} _{-1.24}	0.9 ^{+1.4} _{-0.0}	-2.53 ^{+0.72} _{-0.13}	0.41 ^{+0.27} _{-0.36}	0.34 ^{+0.00} _{-0.09}
PS18kh	5.82 ^{+0.46} _{-0.63}	0.35 ^{+0.41} _{-0.27}	0.9 ^{+1.4} _{-0.0}	-2.64 ^{+0.53} _{-0.08}	0.11 ^{+0.11} _{-0.09}	0.34 ^{+0.00} _{-0.09}
AT2017eqx	5.56 ^{+0.51} _{-0.66}	0.25 ^{+0.31} _{-0.18}	2.5 ^{+0.0} _{-1.4}	-2.67 ^{+0.43} _{-0.06}	0.079 ^{+0.081} _{-0.058}	0.34 ^{+0.00} _{-0.09}
PS1-11af	5.71 ^{+0.52} _{-0.55}	0.28 ^{+0.37} _{-0.20}	0.9 ^{+1.4} _{-0.0}	-2.58 ^{+0.44} _{-0.14}	0.091 ^{+0.097} _{-0.069}	0.34 ^{+0.00} _{-0.09}

^aThe source has two possible solutions and the main one is given at the first entry.

NOTE—Results of the MCMC experiments are obtained with no prior knowledge of BH masses. A uniform prior distribution is adopted for the model parameters, including the BH mass. The uncertainties of model parameters are at the 90-percent confidence level obtained with MCMC experiments.

with the two different methods. The uncertainties of the BH masses calculated with the $M_{\text{BH}}\text{-}\sigma_*$ relation include both the observational uncertainties of the velocity dispersion and the intrinsic scatters of the $M_{\text{BH}}\text{-}\sigma_*$ relation. Figure 10(a) shows that the BH masses of all the TDEs except the TDE iPTF15af obtained with L_p and ΔE are well consistent within about one-standard uncertainties with the BH masses obtained with the $M_{\text{BH}}\text{-}\sigma_*$ relation. The BH mass of TDE iPTF15af obtained with L_p and ΔE is smaller by 0.97-dex or 1.8 times the uncertainties (0.53-dex) than the mass obtained with $M_{\text{BH}}\text{-}\sigma_*$ relation. The UV spectra of TDE iPTF15af have broad absorption lines associated with high-ionization states of N V, C IV, Si IV, and possibly P V, requiring an absorber with column densities $N_{\text{H}} > 10^{23} \text{ cm}^{-2}$ (Blagorodnova et al. 2019). The optically thick gas could significantly absorb the soft X-rays, if present. However, the observations of soft

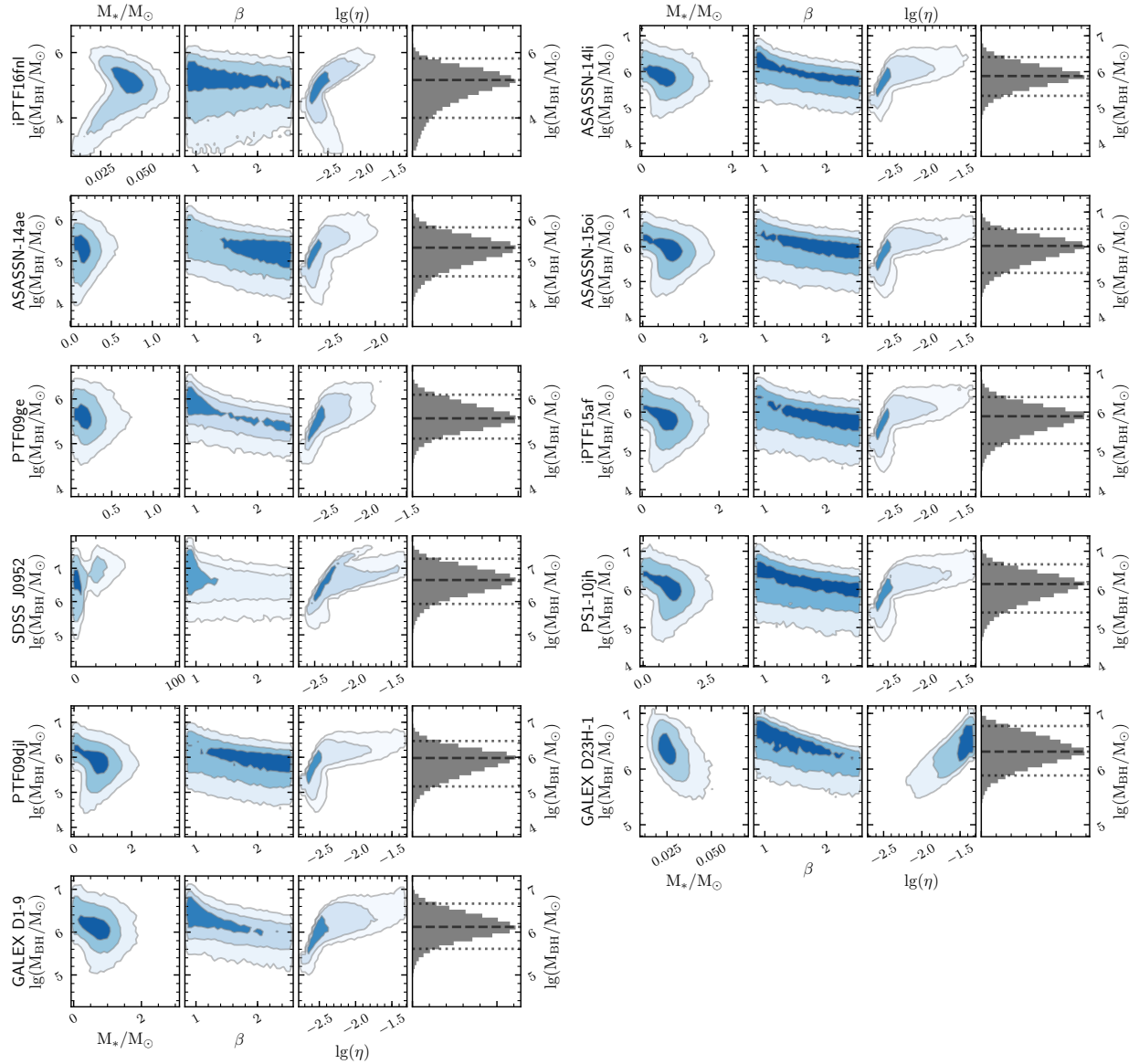


Figure 6. Posterior distributions of model parameters and radiation efficiency of the MCMC experiments. The results are for the TDE sources with observations of stellar velocity dispersion. A uniform prior distribution is adopted for all the model parameters (M_{BH} , M_* and β). Contour plots are for 1, 2, and 3σ . In the histogram of M_{BH} , dashed line indicates the BH mass at the peak of distributions and two dotted lines give the mass ranges at the 90-percent confidence level. The main solution is given if two solutions of a TDE are possible.

X-rays suggested that the radiation of soft X-rays in optically-discovery TDEs are much smaller than or at most comparable to the radiation in optical and UV wavebands and the low value of the BH mass of TDE iPTF15af obtained with L_p and ΔE may not be mainly due to the absorption of soft X-ray radiation but to the intrinsic scatters of the $M_{\text{BH}}-\sigma_*$ relation. In Figure 10(b), we overplot the black hole masses of the TDEs obtained with L_p and ΔE on the $M_{\text{BH}}-\sigma_*$ relation plot of van den Bosch (2016). The data are adopted from Table 2 of van den Bosch (2016), in which the black hole masses are obtained with stellar dynamics, gas dynamics, megamasers and reverberation mapping. For comparison, Figure 10(b) also gives the several popular results of $M_{\text{BH}}-\sigma_*$ relation, which are obtained for all types of galaxies (Ferrarese & Ford 2005;

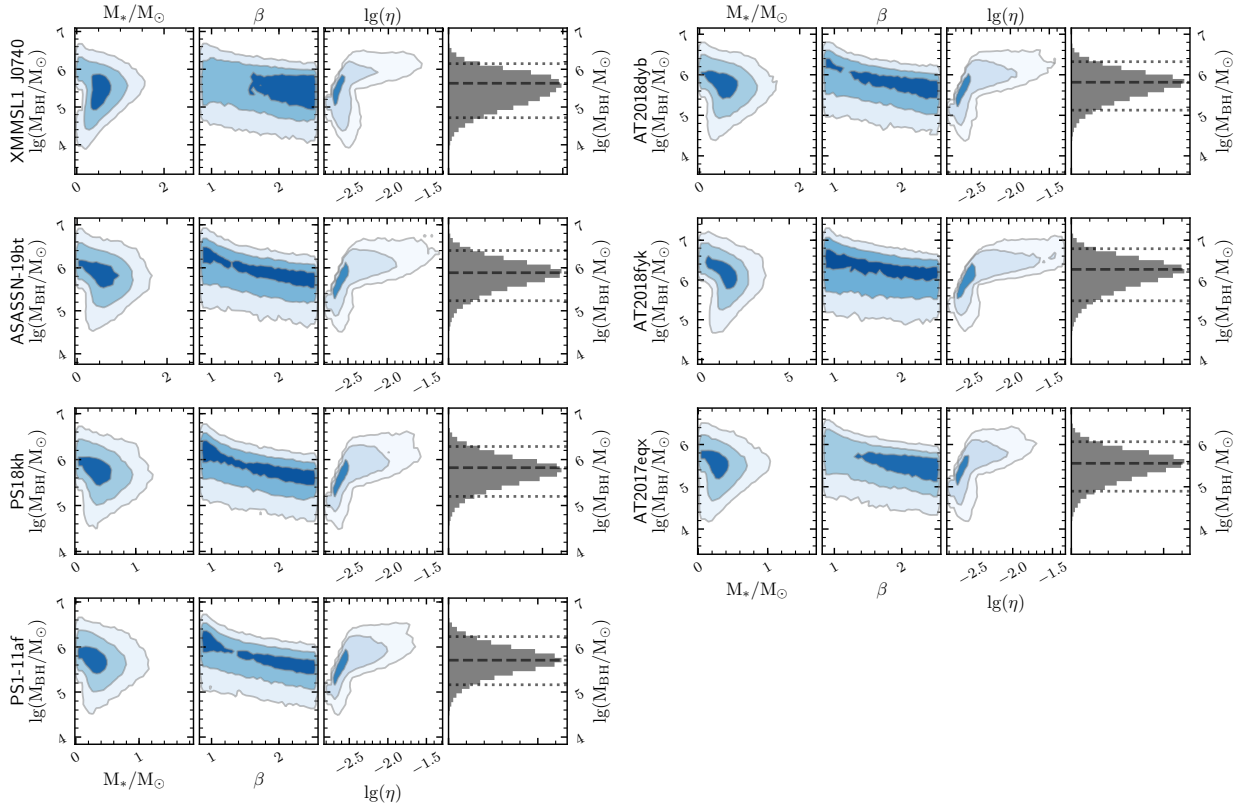


Figure 7. Same as in Figure 6 but for the TDE sources without measurement of stellar velocity dispersions

McConnell & Ma 2013; She et al. 2017) and were recently used to estimate the black hole masses of TDEs in the literature (Stone & Metzger 2016; Wevers et al. 2017, 2019b; Blagorodnova et al. 2017; Leloudas et al. 2019). Kormendy & Ho (2013) only provided an updated $M_{\text{BH}} - \sigma_*$ relation for galaxies with elliptical and classical bulges and the $M_{\text{BH}} - \sigma_*$ relation for all galaxies with the data tabulated by those authors are given only recently (She et al. 2017). Figure 10(b) shows that the $M_{\text{BH}} - \sigma_*$ relation for all galaxies in the literature are nearly identical to each other and the BH masses obtained in this work locate in the core regions of the correlation of the directly measured BH masses and stellar velocity dispersions with a scatter comparable to the intrinsic scatter of the $M_{\text{BH}} - \sigma_*$ relation. In Figure 10(b), the interpolation $M_{\text{BH}} - \sigma_*$ relation of equation (24) is also shown and remarkably consistent with those for all types of galaxies in the literature and the BH masses obtained in this work.

In Sec. 4, we showed observationally and theoretically that the bolometric luminosity and the total radiation energy could properly include the EUV radiation by integrating over a single black body for the optical and UV radiation and adding the observations of soft X-ray wavebands. The consistences of the BH masses obtained in this paper and with the $M_{\text{BH}} - \sigma_*$ relation also suggests that the conclusions are reasonable. However, some deviations of the SEDs of TDEs from the single-temperature blackbody spectrum are occasionally present in the observations of optical/UV TDEs and the contribution of EUV radiation in the bolometric luminosity and the total radiation energy cannot be well constrained until the direct observations of EUV radiation. Here we briefly discuss the effects of the EUV radiation on the results by arbitrarily increasing by 0.5 dex the peak bolometric peak luminosity L_p and the total radiation energy ΔE of the well-known PS1-10j in Table 1, which is equivalent to assume that the EUV radiation is about five times of the

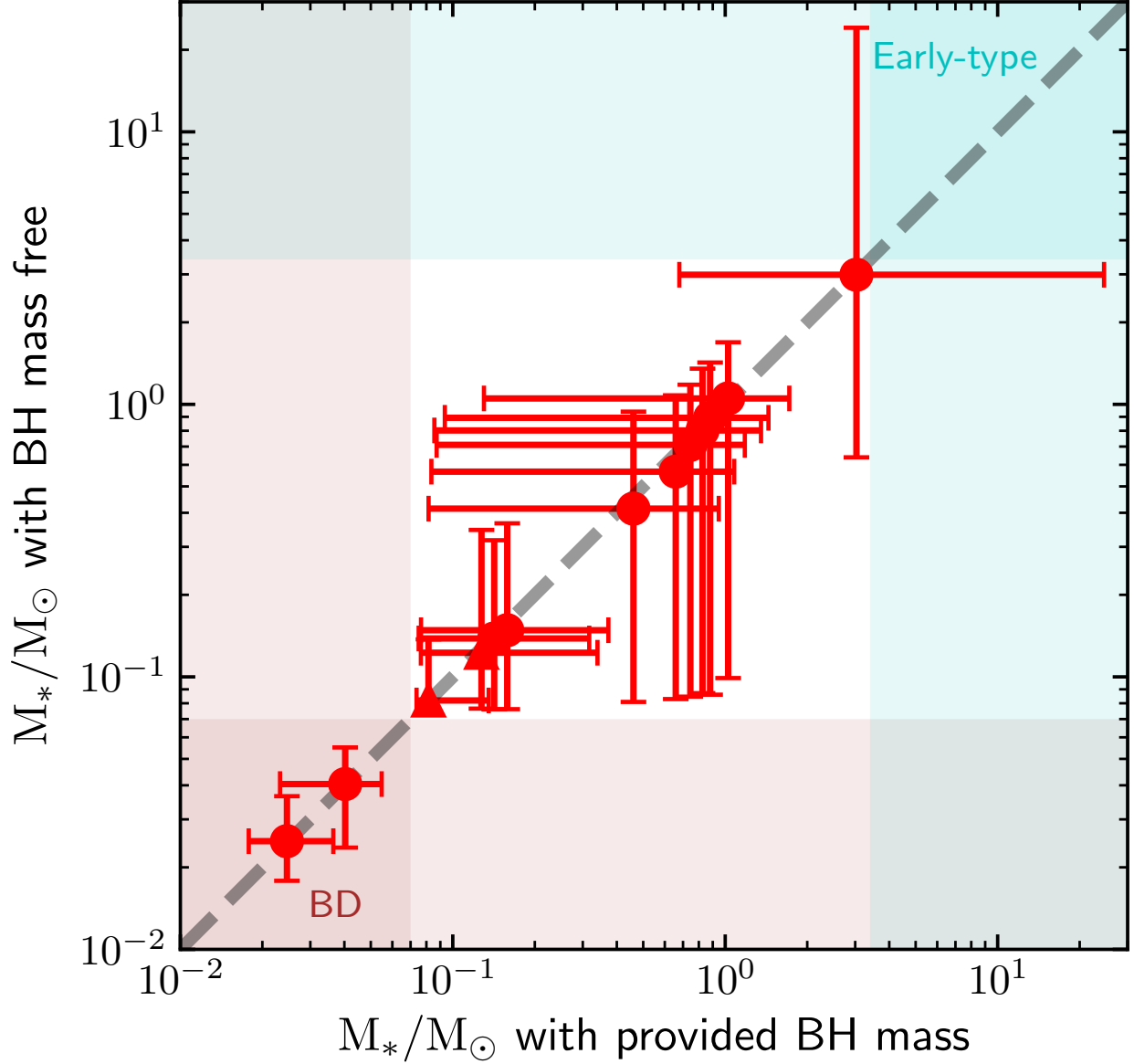


Figure 8. Stellar masses of sample sources with the black hole mass in the MCMC experiment given with the $M_{\text{BH}}-\sigma_*$ relation (x -axis) vs as a free parameter (y -axis). Filled circles are for the main solutions of TDEs and the filled triangle is for the secondary solutions of iPTF16fnl and GALEXD23H-1. The uncertainties are at 90% confidence level obtained with the MCMC experiments. The stellar masses obtained with the two MCMC experiments are well consistent with each other.

observations of the optical/UV wavebands and the color index of the TDE does not significantly change with time. We noticed that the hypothetical bolometric peak luminosity $L_p = 10^{44.84} \text{ erg s}^{-1}$ is about 11 times the Eddington luminosity for BH mass $\lg(M_{\text{BH}}/M_\odot) = 5.71$ given by the $M_{\text{BH}}-\sigma_*$ relation in Table 1 and the hyper-Eddington of peak luminosity leads to the expectation of a top-capped light curve of characteristic Eddington-limited luminosity, which is inconsistent with the observations of PS1-10jh (Gezari et al. 2012). Here we neglect the inconsistency and investigate the effects of the possible missed EUV radiation on the results. With the arbitrarily-assumed bolometric peak luminosity L_p and total radiation energy ΔE , we solve the equations (19) and (21) with the MCMC method. The results give a BH mass $\lg(M_{\text{BH}}/M_\odot) = 6.39^{+0.74}_{-0.82}$,

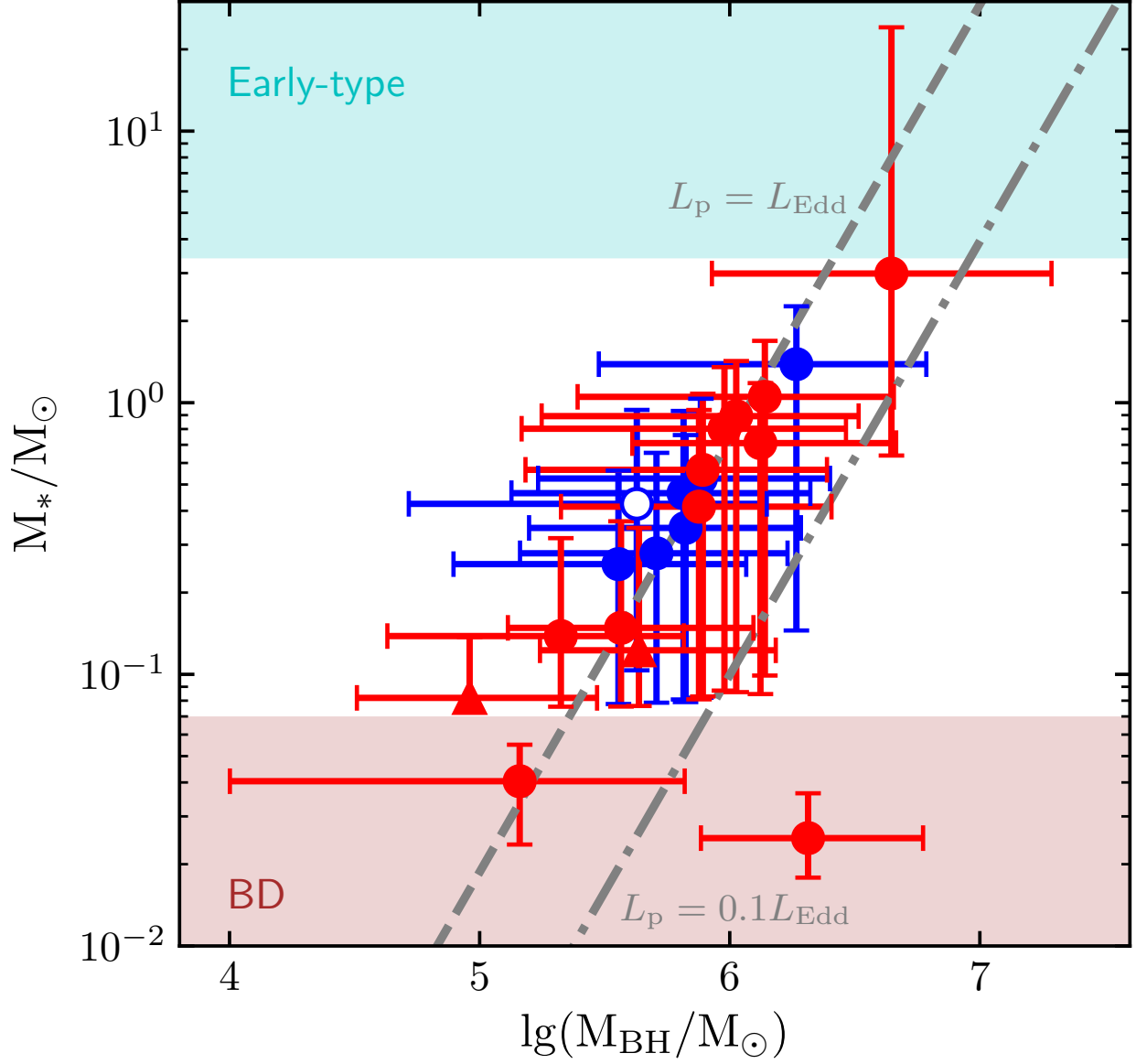


Figure 9. Stellar mass vs black hole mass of the total sample sources. The masses of black hole and star and the associated uncertainties at 90% percent confidence level are calculated with MCMC experiments. The sample sources with and without measurements of stellar velocity dispersion of host galaxy are given with red and blue symbols, respectively. Open circle is the X-ray TDE XMMSL1 J0740 and filled triangles are for the secondary solutions of iPTF16fnl and GALEXD23H-1. The dashed and dash-dotted lines are, respectively, for the observational selection effects of Equation (28) for $L_p = L_{\text{Edd}}$ and $0.1 L_{\text{Edd}}$ (see Sec. 4.3 for detailed discussions).

the star's mass $M_*/M_\odot = 2.87^{+18.75}_{-2.44}$, and the radiation efficiency $\lg(\eta) = -2.46^{+0.50}_{-0.16}$. The results show that a significant increase of the EUV radiation from about one up to about five times the observations in optical/UV would increase the radiation efficiency only by 0.11 dex, the BH mass by 0.25 dex, and the mass of star from $1.05M_\odot$ to $2.87M_\odot$. A star of mass $M_*/M_\odot = 2.87$ is an A-type main sequence star and is roughly consistent with the constraint of the star-formation history of the host galaxy of PS1-10jh on the highest mass of stars evolving off main-sequence (Figure 1 of French et al. 2017). An increase of the peak bolometric luminosity and total radiation energy of PS1-10jh by 0.5 dex would lead to a moderate increase

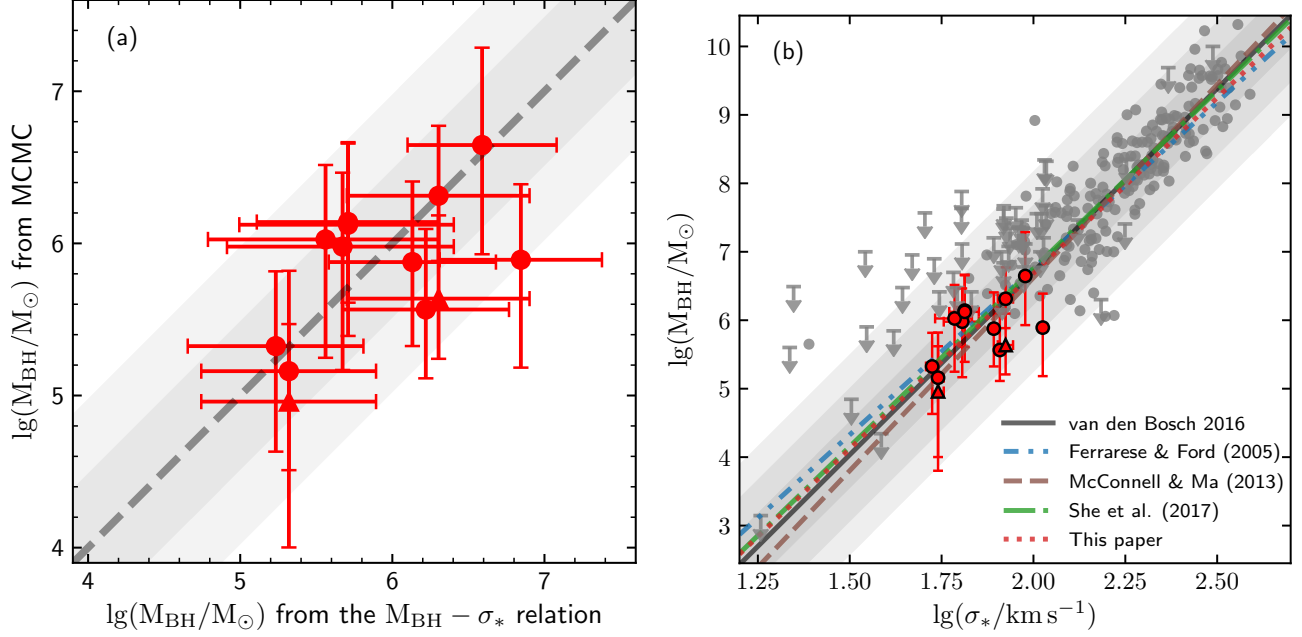


Figure 10. *Left:* Comparison between the black hole mass estimated in this paper (*y-axis*) and with the $M_{\text{BH}} - \sigma_*$ relation (*x-axis*). Dashed line gives the one-to-one relation and dark and light grey regions denote one and two times the intrinsic scatters of the $M_{\text{BH}} - \sigma_*$ relation (van den Bosch 2016). The BH masses obtained with the two different methods are well consistent with each other. *Right:* Correlation between black hole mass and stellar velocity dispersions. BH masses obtained in this paper (red bullets) are over-plotted in the $M_{\text{BH}} - \sigma_*$ relation of van den Bosch (2016), which is derived with the data (dark bullets) in their Table 2. Dark to light gray regions denote one, two, and three times the intrinsic scatters. The lines are the $M_{\text{BH}} - \sigma_*$ relations for all types of galaxies in the literature and the interpolation relation in this paper. The black hole masses of the sample TDE sources obtained in this paper closely follow the $M_{\text{BH}} - \sigma_*$ relation given by the measurements of black hole masses with the stellar dynamics, gas dynamics, megamasers and reverberation mapping.

of the measurement of BH mass by 0.25 dex. The BH mass $\lg(M_{\text{BH}}/M_{\odot}) = 6.39$ is consistent within 2σ with the BH mass $\lg(M_{\text{BH}}/M_{\odot}) = 5.71^{+0.59}_{-0.60}$ obtained with the $M_{\text{BH}} - \sigma_*$ relation. The results show that the EUV radiation, if significant, would not change our conclusions.

5.2. Black hole masses with the $M_{\text{BH}} - M_{\text{bulge}}$ relation

In Sec. 5.1, we computed the BH masses with L_p and ΔE and showed that they are well consistent with the BH masses calculated with the $M_{\text{BH}} - \sigma_*$ relation. In addition to the $M_{\text{BH}} - \sigma_*$ relation, the BH masses can also be calculated with the bulge mass M_{bulge} of host galaxies with the $M_{\text{BH}} - M_{\text{bulge}}$ relation (Magorrian et al. 1998) and the $M_{\text{BH}} - M_{\text{bulge}}$ relation for classical bulges and ellipticals has the same intrinsic scatter as the $M_{\text{BH}} - \sigma_*$ relation (Häring & Rix 2004; Kormendy & Ho 2013). However, it is noticed in the literature that the BH masses of TDEs derived with the $M_{\text{BH}} - M_{\text{bulge}}$ relations are systematically higher than those obtained with the $M_{\text{BH}} - \sigma_*$ relation (Wevers et al. 2017; Gezari et al. 2017; Mockler et al. 2019) and the BH masses of AGNs are also an order of magnitude smaller than those calculated with the $M_{\text{BH}} - M_{\text{bulge}}$ relation. There are several possible explanations for the discrepancy: (1) TDEs are expected to occur in dwarf galaxies and it is difficult to spatially resolve the bulge of the host galaxies of TDEs and to obtain accurate estimate of the bulge mass and (2) the host galaxies of most TDEs are E+A galaxies or post-starburst galaxies (Arcavi

et al. 2014; French et al. 2016), which are in transition between late-type spirals and passive early-type galaxies and have central overdensity of star with reference to the galaxies deriving the $M_{\text{BH}}-M_{\text{bulge}}$ relation (French et al. 2017). It was recently suggested that the BH masses of TDEs obtained with the $M_{\text{BH}}-M_{\text{bulge}}$ and $M_{\text{BH}}-\sigma_*$ relations may be roughly consistent with each other, if the $M_{\text{BH}}-M_{\text{bulge}}$ relation for all types of host galaxies are used and the B/T ratio of host galaxies of TDEs are estimated with the relation of the total stellar mass of galaxies and the B/T ratio averaged over all types of galaxies (Wevers et al. 2019b). Here we follow the approach to estimate the BH masses. We estimate the B/T ratio of host galaxies of the TDE sample sources using the empirical relation of the total stellar mass of galaxy and the averaged bulge-to-total mass ratio (B/T) obtained for all types of galaxies (Stone et al. 2018). The results of the ratio B/T are given in Table 1 and have very large uncertainties. Following Wevers et al. (2019b), we estimate the BH masses of the TDE sample sources using the $M_{\text{BH}}-M_{\text{bulge}}$ relation for total galaxies (Häring & Rix 2004). In Fig. 11 we overplot the BH masses obtained with the $M_{\text{BH}}-M_{\text{bulge}}$ relation on the $M_{\text{BH}}-M_{\text{BH}}$ plot. Because it is difficult to estimate the uncertainties of the total stellar masses and the ratio B/T, the uncertainties of the BH masses obtained with the $M_{\text{BH}}-M_{\text{bulge}}$ relation in Fig. 11 include only the intrinsic scatters of the $M_{\text{BH}}-M_{\text{bulge}}$ relation and the real uncertainties of the BH masses are much larger than the ones quoted here. After taking into account of the large uncertainties of the BH masses, Fig. 11 shows that the BH masses with the $M_{\text{BH}}-M_{\text{bulge}}$ relation are largely consistent with the BH masses obtained from L_p and ΔE in this paper and from the $M_{\text{BH}}-\sigma_*$ relation, although a small systematic difference may be possible.

It is well known that the BHs in quiescent galaxies do not correlate with galaxy disks (Kormendy & Ho 2013, and references therein). It was shown recently that the BH masses of local AGNs may correlate with the total stellar mass of host galaxies M_{tot} with an intrinsic scatter 0.55 dex (Reines & Volonteri 2015). The relation of BH masses and total stellar masses of host galaxies of AGNs is used to estimate the BH masses of TDEs in the literature in particularly when the observations of stellar velocity dispersions of TDEs is not available (e.g. Komossa et al. 2004; Gezari et al. 2017; Lin et al. 2017a,b). We calculate the BH masses of the TDE sources with the total stellar masses of host galaxies in Table 1 and the $M_{\text{BH}}-M_{\text{tot}}$ relation (Reines & Volonteri 2015) and give the results in Table 1. We overplot the results of BH masses on the $M_{\text{BH}}-M_{\text{BH}}$ plot in Fig. 11. Fig. 11 shows that the BH masses with the $M_{\text{BH}}-M_{\text{tot}}$ relation are broadly consistent with both the BH masses obtained in this paper and with the $M_{\text{BH}}-\sigma_*$ relation, although a small systematic difference cannot be excluded.

5.3. BH masses obtained by fitting the light curves of TDEs

In this paper we suggest to measure the masses of BHs and stars of TDEs by jointly fitting the observations of the peak bolometric luminosity and the total radiation energy with the peak fallback rate of matter and the total accreted material. In the calculations, we use the conversion efficiency of matter into radiation with the elliptical accretion disk model suggested in Liu et al. (2017). Mockler et al. (2019) recently proposed to measure the BH masses by fitting the well observed light curves of TDEs with the simulations of the fallback rate of stellar debris (Guillochon & Ramirez-Ruiz 2013). In the calculations the conversion efficiency of matter into radiation is assumed to be a constant free parameter of agnostic physics origin (Mockler et al. 2019).

Figure 12 plots the BH masses of the TDEs obtained in this work and in Mockler et al. (2019). We do not compare the masses of star of TDEs obtained with the two methods, because the fitting of light curves cannot give constraints of the stellar mass due to the strong degeneracy of stellar mass and the orbital penetration factor (Mockler et al. 2019). In Figure 12, we overplot the BH mass obtained with the $M_{\text{BH}}-\sigma_*$ relation for comparison. Figure 12 shows that the BH masses obtained by fitting the light curves are roughly

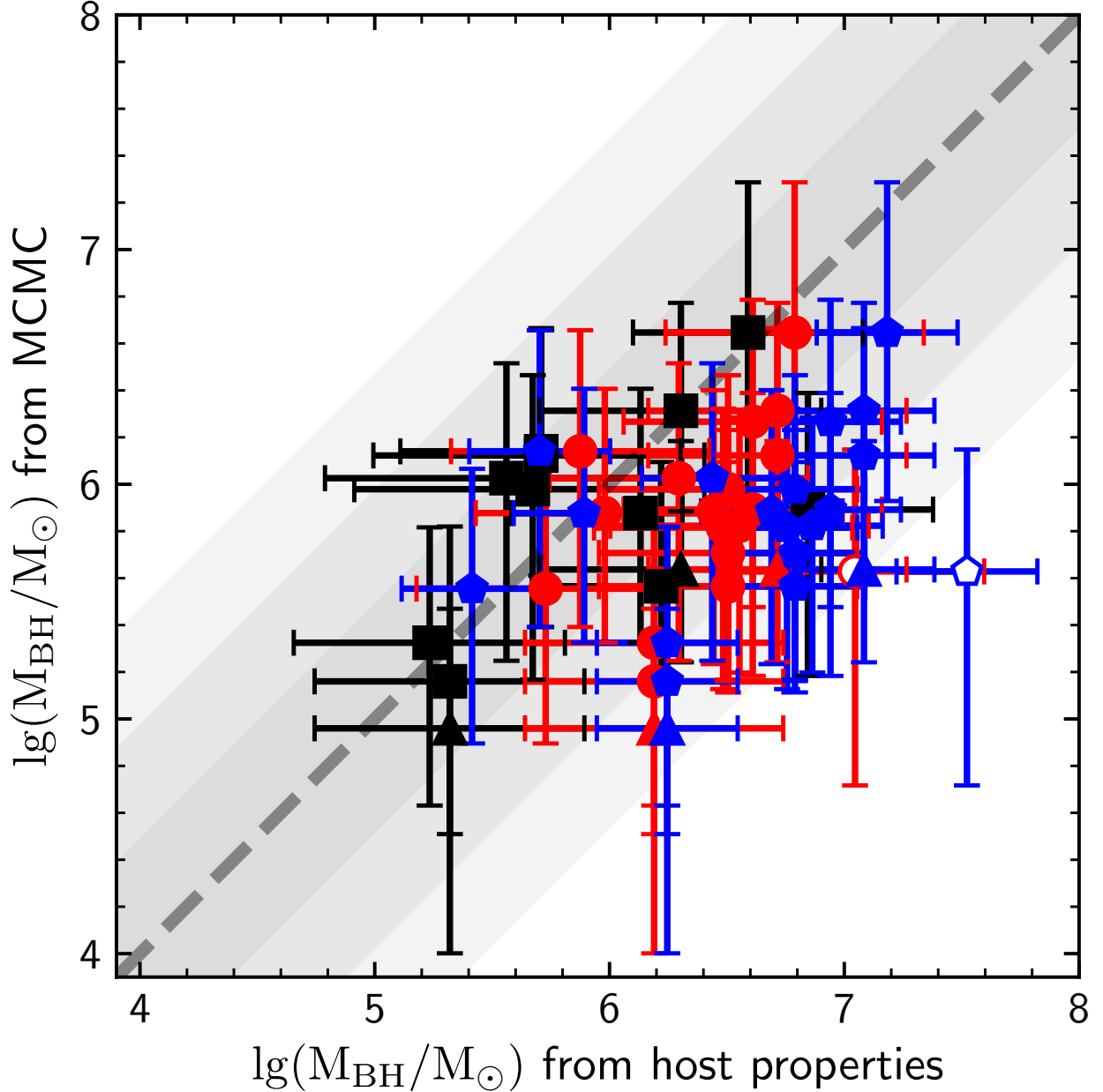


Figure 11. Comparison between the black hole masses obtained in this paper (*y-axis*) and with the total and bulge masses of host galaxy (*x-axis*). Filled pentagon is for BH masses obtained with the $M_{\text{BH}}-M_{\text{bulge}}$ relation. Results obtained with the $M_{\text{BH}}-M_{\text{tot}}$ relation are given with filled circles. The open pentagon and open circle are for the X-ray TDE XMMSL1 J0740. The BH masses calculated with the $M_{\text{BH}}-\sigma_*$ relation are over-plotted with filled square for comparison. Filled triangle is for the secondary solutions of iPTF16fnl and GALEXD23H-1. Dashed line is the one-to-one relation and the dark to light grey regions give one, two and three times the intrinsic scatter of the $M_{\text{BH}}-\sigma_*$ relation.

consistent with the BH mass obtained with L_p and ΔE and the $M_{\text{BH}}-\sigma_*$ relation, although it is clear that the BH masses obtained by fitting the light curves of TDEs would give systematically larger BH masses than both our method and the $M_{\text{BH}}-\sigma_*$ relation. It has already noted in the literature that the method of fitting the light curves systematically higher black hole masses than the $M_{\text{BH}}-\sigma_*$ relation (Mockler et al. 2019). Among

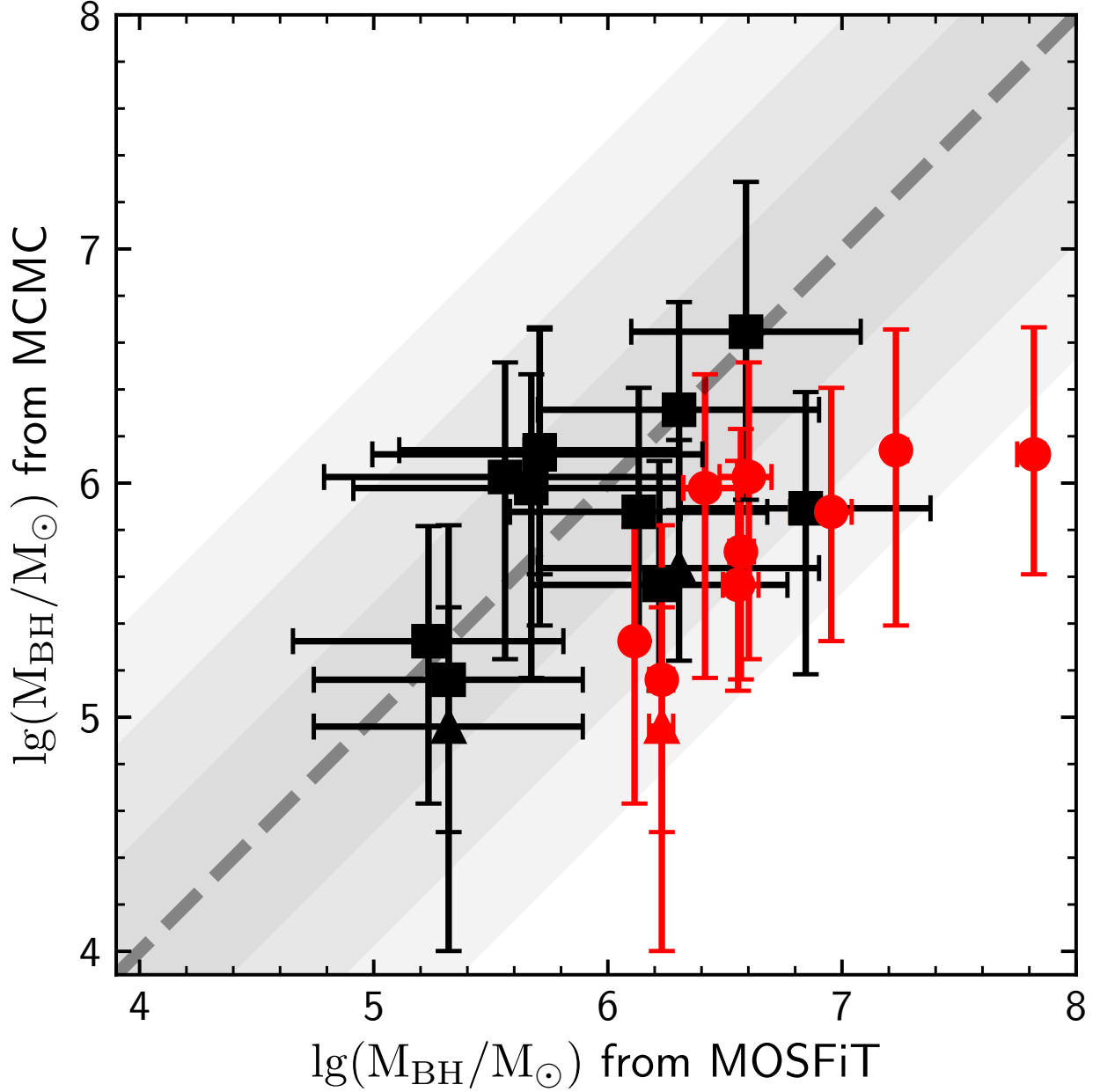


Figure 12. Comparison of the black hole masses obtained in this paper (*y-axis*) and with fitting the multiwavelength light curves of TDEs (Mockler et al. 2019) (*x-axis*). BH masses calculated with the $M_{\text{BH}}-\sigma_*$ relation are over-plotted with filled square for comparison. Dashed line is the one-to-one relation and the dark to light grey regions give one, two and three times the intrinsic scatter of the $M_{\text{BH}}-\sigma_*$ relation. The BH masses measured with the different observational properties of TDEs are largely consistent with each other.

all the sample sources, the TDE GALEX D1-9 has the largest difference of BH masses. The fit of the light curve of GALEX D1-9 gives the BH mass about $6.6 \times 10^7 M_\odot$ (Mockler et al. 2019), about two orders of magnitude larger than that ($10^{5.71} M_\odot$) obtained with the $M_{\text{BH}}-\sigma_*$ relation and about fifty times larger than the measurement $10^{6.12} M_\odot$ in this paper.

6. DISCUSSION AND CONCLUSION

Liu and colleagues recently suggested that the accretion disk of TDEs is large and highly eccentric and the orbital eccentricity of the disk fluid elements remain nearly constant during the accretion onto the black hole (Liu et al. 2017; Cao et al. 2018). Here we calculated the radiation efficiency of the elliptical accretion disk model for TDEs. Our results show that the radiation efficiency of highly eccentric accretion disk depends on the masses of black hole and star and the orbital penetration factor of star and would significantly vary with TDEs. The radiation efficiency of the elliptical accretion disk model could be as small as 10^{-3} , or about two orders of magnitude smaller than the typical radiation efficiency $\eta = 0.1$ adopted for TDEs in the literature. Based on the elliptical accretion disk model, we calculate the expected peak luminosity and total radiation energy after peak of TDEs, which can be well determined observationally.

We compile from the literature the observational data of peak bolometric luminosity and total radiation energy after peak of a sample of 18 non-jetted TDEs in quiescent galaxies. Among the 18 sample TDE sources, 11 TDEs have available measurements of the stellar velocity dispersion of host galaxy and the black hole masses are calculated with the $M_{\text{BH}} - \sigma_*$ relation. We show that the expectations and observations of the peak bolometric luminosity and total radiation energy of TDEs are well consistent with each other. The low peak luminosity and small mass accretion of TDEs are due to the unusually low radiation efficiency of elliptical accretion disk and require neither alternative explanations for the transient sources (e.g. Saxton et al. 2018) nor a miss of major released energy in extreme-UV (e.g. Lu & Kumar 2018).

Provided L_p and ΔE , we uniquely determined the mass of star through the equations (19) and (21) and calculated the radiation efficiency of the sample TDE sources with and without the provided black hole mass using the MCMC experiments. The radiation efficiency is generally a free parameter of agnostic origin in modeling the observations of TDEs in the literature (e.g. Liu et al. 2014; Mockler et al. 2019). Based on the properties of the accretion disk obtained by modeling the profiles of the broad optical emission lines, the radiation efficiency of the TDE PTF09djl and ASASSN-14li are given, respectively, $\lg \eta \simeq -2.38$ (Liu et al. 2017) and $\lg \eta \simeq -2.43$ (Cao et al. 2018), well consistent with the results $\lg \eta = -2.61_{-0.10}^{+0.58}$ for PTF09djl and $\lg \eta = -2.57_{-0.14}^{+0.54}$ for ASASSN-14li in this paper. The radiation efficiencies of a sample of TDEs are recently obtained by fitting the light curves with the fallback rate of stellar debris (MOSFiT, Mockler et al. 2019). However, the uncertainties of the MOSFiT results are very large because the radiation efficiency with MOSFiT method is strongly degenerate with the stellar mass ranging from $0.01M_\odot$ to $100M_\odot$ and cannot be determined uniquely. As an example, Table 5 of Mockler et al. (2019) gave the results of the TDE PS1-10jh obtained with different stellar masses. They showed that the radiation efficiency changes from $\eta = 0.9 \times 10^{-1}$ for $M_* = 0.1M_\odot$, through $\eta = 3.8 \times 10^{-3}$ for $M_* = 1.0M_\odot$, to $\eta = 4 \times 10^{-4}$ for $M_* = 10M_\odot$. No strong prior can be given to the stellar mass and the uncertainty of the radiation efficiency of PS1-10jh obtained with the MOSFiT method can be as large as up to about 3 dex, which is much larger than the quoted uncertainty of the fiducial value $\eta = 0.09_{-0.02}^{+0.03}$ (Mockler et al. 2019). In this paper, the stellar mass and radiation efficiency of TDE PS1-10jh can be uniquely determined and from Table 2 are $M_* = 1.02_{-0.89}^{+0.69}M_\odot$ and $\lg(\eta) = -2.55_{-0.13}^{+0.68}$. Our results are significantly smaller than the fiducial value of the MOSFiT method. Interestingly, our results are well consistent with the test result of $M_* = 1.0M_\odot$ and $\eta = 3.8 \times 10^{-3}$ (or $\lg \eta = -2.42$) of the MOSFiT method. With the caveats of the large systematic uncertainties with the results of MOSFiT method, we conclude that the radiation efficiencies obtained in this paper and with the MOSFiT method may be consistent with each other. The low radiation efficiency of typical value obtained with the elliptical accretion disk model of Liu et al. (2017) is reasonable. The sample of TDE sources except TDE GALEX D23H-1 have a typical radiation efficiency $\eta \simeq 2.7 \times 10^{-3}$, which is about 37 times smaller than the typical radiation efficiency $\eta = 0.1$ adopted for TDEs in the literature.

With provided total radiation energy, a low radiation efficiency implies a large accreted matter onto black hole. We calculate the amount of accreted stellar matter after peak and its ratio to the mass of star and show that the accreted matter after peak of the sample TDE sources are in the range of about $10^{-2}M_{\odot}$ to $0.97M_{\odot}$ and are about 34% of the mass of star. The fraction 34% is the expectation of hydrodynamic simulations of tidal disruption of low mass star with polytropic index $\gamma = 5/3$ and orbital penetration factor $\beta \sim 1$. Our model does not calculate the accreted matter before peak and we cannot estimate the total accreted stellar matter of TDEs. Because the total radiation energy before peak is significant, the total accreted matter could be up to about half of the mass of star, consistent with the expectation of total accretion of the tidal disruption of star. The results imply that most of the orbital kinematic energy of the stellar debris is advected onto the BH instead of being converted into radiation and emitting in EUV, as suggested in the literature (e.g. [Lu & Kumar 2018](#)), and that the low peak bolometric luminosity and total radiation energy or the apparent accreted matter of the optical/UV nuclear transients do not require an alternative explanation as suggested in [Saxton et al. \(2018\)](#).

The star of the sample TDE sources except SDSS J0952+2143 has mass in the range of $M_{*} \simeq 2.5 \times 10^{-2}M_{\odot}$ and $1.4M_{\odot}$ and a spectral type ranging from brown dwarfs to late A-type main sequence. The absence of B and O type stars of the TDE sample sources is consistent with the observations that the host galaxies of most TDEs are E+A galaxies and have a burst of star formation in a few Gig-years ago ([Arcavi et al. 2014](#); [French et al. 2016](#)). The mass of the star of the TDE SDSS J0952+2143 is about $3.0M_{\odot}$ and consistent with that the host galaxy of TDE SDSS J0952+2143 is a star-forming galaxy of rich young stars ([Palaversa et al. 2016](#)).

With the observations of the peak bolometric and the total radiation energy after peak, we can uniquely determine the masses of black holes of the sample TDE sources. The black hole masses of TDEs obtained in this paper are consistent with those obtained with the classical $M_{\text{BH}} - \sigma_{*}$, $M_{\text{BH}} - M_{\text{bulge}}$, and $M_{\text{BH}} - M_{\text{tot}}$ relations. It was noticed in the literature that the black hole masses of TDEs given with the $M_{\text{BH}} - L_{\text{bulge}}$ or $M_{\text{BH}} - M_{\text{bulge}}$ relation are much larger than those calculated with the $M_{\text{BH}} - \sigma_{*}$ relation. Our results suggest that the discrepancy of the measurements of the black hole masses of TDEs obtained with the two classical relations of black hole mass and the properties of host galaxies are most probably due to the difficulties to accurately measure the mass of the bulge of host galaxies.

The black hole masses of many of our sample TDE sources were recently calculated by analyzing the multi-waveband light curves with MOSFiT method ([Mockler et al. 2019](#)). The black hole masses of the TDEs obtained in this paper and with MOSFiT are largely consistent with each other with some exceptions. The black hole mass measurement with MOSFiT method gives $M_{\text{BH}} = 6.6 \times 10^7 M_{\odot}$ for GALEX D1-9 and $M_{\text{BH}} = 1.7 \times 10^7 M_{\odot}$ for PS1-10jh ([Mockler et al. 2019](#)), which are, respectively, about 50 times and 12 times larger than the measurements of $10^{6.14}M_{\odot}$ and $10^{6.12}M_{\odot}$ in this paper. It has also been noticed in the literature ([Wevers et al. 2017, 2019b](#)) and in this paper that the measurements of the black hole masses of GALEX D1-9 and TDE PS1-10jh with MOSFiT are, respectively, much larger than the measurement of $10^{5.71}M_{\odot}$ calculated with the $M_{\text{BH}} - \sigma_{*}$ relation. The black hole mass in the MOSFiT method is determined primarily by fitting the rising-to-peak timescale of the multi-waveband light curves with the expected time of peak fallback rate with the assumption of prompt circularization of the bound debris streams ([Mockler et al. 2019](#)). However, a prompt circularization of stellar debris streams and rapid formation of accretion disk are expected only for tidal disruptions of star with orbital pericenter about the gravitational radius of black hole and a slow circularization of debris streams is expected for tidal disruptions of star by black hole of mass $\sim 10^6 M_{\odot}$ and with penetration factor $\beta \sim 1$ ([Shiokawa et al. 2015](#); [Bonnerot et al. 2016](#); [Hayasaki](#)

& Loeb 2016; Dai et al. 2015). Provided the rising-to-peak timescale of the light curves of TDEs, a slower circularizations of debris stream leads to a shorter timescale of peak fallback rate and would results in a smaller mass of black hole.

Among the 18 sample TDE sources, eleven have the measurements of stellar velocity dispersion of host galaxies. When the black hole masses obtained in this paper are over-plotted on the $M_{\text{BH}} - \sigma_*$ diagram of the black hole masses measured with the stellar dynamics, gas dynamics, megamasers and reverberation mapping, the black hole masses obtained in this paper share the same $M_{\text{BH}} - \sigma_*$ relation as the black hole masses measured with direct methods and distributes at the low mass region of the $M_{\text{BH}} - \sigma_*$ diagram. The results indicate that the method in this paper can give an independent measurements of black hole mass as accurately as the dynamic methods and test the $M_{\text{BH}} - \sigma_*$ relation at low black hole mass. We have calculated the black hole masses of the 7 sample TDE sources without measurement of stellar velocity dispersions of host galaxies. It would be interesting to observe the stellar velocity dispersion of host galaxies and compare the masses of black hole obtained in this paper and the $M_{\text{BH}} - \sigma_*$ relation in the future.

The measurements of the masses of black holes and stars of TDEs obtained in this paper are determined mainly by the absolute peak brightness and the total radiation energy integrated over the light curves after peak and depend very weakly on either the shapes of the light curves or the properties of star. The well consistences between the black hole masses of the sample TDE sources obtained in this paper and with the $M_{\text{BH}} - \sigma_*$ relation and between the fractions of accreted stellar mass inferred in this paper and the expectation of the hydrodynamic simulations of stellar tidal disruptions well justify the elliptical accretion disk model of large size and invariant extreme eccentricity (Liu et al. 2017; Cao et al. 2018). An elliptical accretion disk of large size and extreme eccentricity usually has a sub-Eddington luminosity for black hole of mass $\gtrsim 10^6 M_\odot$ and is significantly super-Eddington only for tidal disruption of main-sequence star by intermediate mass black holes with mass $M_{\text{BH}} \lesssim 10^5 M_\odot$. An accretion disk of sub-Eddington luminosity is cool and radiatively efficient and emits luminosity closely following the fallback rate of stellar debris. A large and extremely eccentric accretion disk emits energy peaking at the optical/UV wavebands with typical temperature $T \sim 10^4$ K and has an emission region of about the semimajor axis of the most bound stellar debris a_{mb} (Liu et al. 2017; Cao et al. 2018). The radiation of the elliptical accretion disk are consistent with the observations of optical/UV TDEs and no optically thick envelope is needed. No strong disk wind or outflow is expected to form in the surface of a cool sub-Eddington accretion disk. However, a small fraction of fallback matter may become unbound and form outflows due to the shocks of the stream collisions at the apogee of the elliptical disk (Jiang et al. 2016) and absorptions may be detected in the spectra of some TDEs.

7. SUMMARY

We have calculated the radiation efficiency of the elliptical accretion disk model for TDEs and investigated its implications of the observations of TDEs. We showed that the low peak bolometric luminosity and small total radiation energy of TDEs result from the low radiation efficiency of the elliptical accretion disk. Provided the observations of the peak bolometric luminosity and the total radiation energy after peak, we can derive the masses of the black holes and stars of TDEs, because the peak bolometric luminosity and the total radiation energy depend on the masses of BHs and stars and are nearly independent of the penetration factor for TDEs with $0.7 \lesssim \beta \lesssim 2.1$ and $M_{\text{BH}} \lesssim 10^{6.5} M_\odot$. While for TDEs with $\beta \gtrsim 2.5$ or $M_{\text{BH}} \gtrsim 10^{6.7} M_\odot$, the masses of the black holes and the orbital penetration factor can be well determined, because the peak bolometric luminosity and the total radiation energy depend on the mass of BHs and the penetration factor and are nearly independent of the mass of star.

As the method in this paper does not require the knowledge of the properties of the host galaxies, it can be used to measure the masses of off-center recoiling BHs and galaxy mergers, the masses of the intermediate mass black hole in globular star clusters, or the masses of primordial BHs wandering in galactic disks or halo. Having an alternative BH mass estimation is also of great interest for classical galaxies with central SMBHs, because (1) in dwarf galaxies, accurate σ_* measurements require deep exposures with very high spectral resolution, (2) σ_* measurements become more difficult for high- z sources, and (3) upcoming and next-generation sky surveys are expected to detect TDEs in the 1000s, and high-sensitivity high-resolution optical follow will rarely be feasible for so many sources. Finally, we would like to emphasize again that BH-host scaling relations have been little explored below BH masses of $\sim 10^6 M_\odot$, and TDEs offer an excellent chance to explore this further once found in large numbers in the future.

ACKNOWLEDGEMENTS

We would like to thank Hua Gao, Julian Krolik, Nadejda Blagorodnova, Richard Saxton, and Thomas Wevers for helpful discussions. This work is supported by the National Natural Science Foundation of China (NSFC11473003, No.11721303) and the Strategic Priority Research Program of the Chinese Academy of Sciences (Grant No. XDB23010200 and No. XDB23040000). LCH was supported by the National Key R&D Program of China (2016YFA0400702).

Software: Astropy (Astropy Collaboration et al. 2013), emcee (Foreman-Mackey et al. 2013), lmfit (Newville et al. 2014), Matplotlib (Hunter 2007), NumPy (van der Walt et al. 2011), Pandas (McKinney 2010) and SciPy (Jones et al. 2001–).

REFERENCES

- Abramowicz, M. A., Czerny, B., Lasota, J. P., & Szuszkiewicz, E. 1988
- Abramowicz, M. A., Jaroszynski, M., & Sikora, M. 1978, *A&A*, 63, 221
- Arcavi, I., Gal-Yam, A., Sullivan, M., et al. 2014, *ApJ*, 793, 38
- Astropy Collaboration, Robitaille, T. P., Tollerud, E. J., et al. 2013, *A&A*, 558, A33
- Bell, E. F., McIntosh, D. H., Katz, N., & Weinberg, M. D. 2003, *ApJS*, 149, 289
- Blagorodnova, N., Cenko, S. B., Kulkarni, S. R., et al. 2019, *ApJ*, 873, 92
- Blagorodnova, N., Gezari, S., Hung, T., et al. 2017, *ApJ*, 844, 46
- Bonnerot, C., Rossi, E. M., Lodato, G., & Price, D. J. 2016, *MNRAS*, 455, 2253
- Bright, J. S., Fender, R. P., Motta, S. E., et al. 2018, *MNRAS*, 475, 4011
- Brown, J. S., Holoien, T. W.-S., Auchettl, K., et al. 2017, *MNRAS*, 466, 4904
- Brown, J. S., Kochanek, C. S., Holoien, T. W.-S., et al. 2018, *MNRAS*, 473, 1130
- Cao, R., Liu, F. K., Zhou, Z. Q., Komossa, S., & Ho, L. C. 2018, *MNRAS*, 480, 2929
- Cappelluti, N., Ajello, M., Rebusco, P., et al. 2009, *A&A*, 495, L9
- Chabrier, G., & Baraffe, I. 2000, *ARA&A*, 38, 337
- Chen, K., & Halpern, J. P. 1989, *ApJ*, 344, 115
- Chen, K., Halpern, J. P., & Filippenko, A. V. 1989, *ApJ*, 339, 742
- Chen, X., Liu, F. K., & Magorrian, J. 2008, *ApJ*, 676, 54
- Chen, X., Madau, P., Sesana, A., & Liu, F. K. 2009, *ApJL*, 697, L149
- Chornock, R., Berger, E., Gezari, S., et al. 2014, *ApJ*, 780, 44
- Cox, A. N. 2000, *Allen's astrophysical quantities*
- Dai, L., McKinney, J. C., & Miller, M. C. 2015, *ApJL*, 812, L39
- Dai, L., McKinney, J. C., Roth, N., Ramirez-Ruiz, E., & Miller, M. C. 2018, *ApJL*, 859, L20
- Donato, D., Cenko, S. B., Covino, S., et al. 2014, *ApJ*, 781, 59
- Eracleous, M., & Halpern, J. P. 1994, *ApJS*, 90, 1

- Eracleous, M., & Halpern, J. P. 2003, *ApJ*, 599, 886
- Esquej, P., Saxton, R. D., Komossa, S., et al. 2008, *A&A*, 489, 543
- Evans, C. R., & Kochanek, C. S. 1989, *ApJL*, 346, L13
- Ferrarese, L., & Ford, H. 2005, *SSRv*, 116, 523
- Ferrarese, L., & Merritt, D. 2000, *ApJL*, 539, L9
- Foreman-Mackey, D., Hogg, D. W., Lang, D., & Goodman, J. 2013, *PASP*, 125, 306
- French, K. D., Arcavi, I., & Zabludoff, A. 2016, *ApJL*, 818, L21
- French, K. D., Arcavi, I., & Zabludoff, A. 2017, *ApJ*, 835, 176
- Gao, H., Ho, L. C., Barth, A. J., & Li, Z.-Y. 2019, *ApJS*, 244, 34
- Gebhardt, K., Bender, R., Bower, G., et al. 2000, *ApJL*, 539, L13
- Gezari, S., Basa, S., Martin, D. C., et al. 2008, *ApJ*, 676, 944
- Gezari, S., Cenko, S. B., & Arcavi, I. 2017, *ApJL*, 851, L47
- Gezari, S., Chornock, R., Rest, A., et al. 2012, *Nature*, 485, 217
- Gezari, S., Heckman, T., Cenko, S. B., et al. 2009, *ApJ*, 698, 1367
- Gezari, S., Martin, D. C., Milliard, B., et al. 2006, *ApJL*, 653, L25
- Golightly, E. C. A., Nixon, C. J., & Coughlin, E. R. 2019, *ApJL*, 882, L26
- Graham, A. W., Onken, C. A., Athanassoula, E., & Combes, F. 2011, *MNRAS*, 412, 2211
- Graur, O., French, K. D., Zahid, H. J., et al. 2018, *ApJ*, 853, 39
- Guillochon, J., Manukian, H., & Ramirez-Ruiz, E. 2014, *ApJ*, 783, 23
- Guillochon, J., & Ramirez-Ruiz, E. 2013, *ApJ*, 767, 25
- Halpern, J. P., Gezari, S., & Komossa, S. 2004, *ApJ*, 604, 572
- Häring, N., & Rix, H.-W. 2004, *ApJL*, 604, L89
- Hayasaki, K., & Loeb, A. 2016, *Scientific Reports*, 6, 35629
- Hayasaki, K., Stone, N., & Loeb, A. 2013, *MNRAS*, 434, 909
- Hills, J. G. 1975, *Nature*, 254, 295
- Holoien, T. W.-S., Brown, J. S., Auchettl, K., et al. 2018, *MNRAS*, 480, 5689
- Holoien, T. W.-S., Huber, M. E., Shappee, B. J., et al. 2019a, *ApJ*, 880, 120
- Holoien, T. W.-S., Kochanek, C. S., Prieto, J. L., et al. 2016a, *MNRAS*, 455, 2918
- Holoien, T. W.-S., Kochanek, C. S., Prieto, J. L., et al. 2016b, *MNRAS*, 463, 3813
- Holoien, T. W.-S., Prieto, J. L., Bersier, D., et al. 2014, *MNRAS*, 445, 3263
- Holoien, T. W. S., Valley, P. J., Auchettl, K., et al. 2019b, arXiv e-prints, arXiv:1904.09293
- Hung, T., Cenko, S. B., Roth, N., et al. 2019, arXiv e-prints, arXiv:1903.05637
- Hung, T., Gezari, S., Blagorodnova, N., et al. 2017, *ApJ*, 842, 29
- Hunter, J. D. 2007, *Computing in Science and Engineering*, 9, 90
- Jiang, Y.-F., Guillochon, J., & Loeb, A. 2016, *ApJ*, 830, 125
- Jones, E., Oliphant, T., Peterson, P., et al. 2001–, *SciPy: Open source scientific tools for Python*
- Jonker, P. G., Stone, N. C., Generozov, A., van Velzen, S., & Metzger, B. 2019, arXiv e-prints, arXiv:1906.12236
- Kippenhahn, R., Weigert, A., & Weiss, A. 2012, *Stellar Structure and Evolution*
- Kochanek, C. S. 1994, *ApJ*, 422, 508
- Kochanek, C. S. 2016, *MNRAS*, 458, 127
- Komossa, S. 2015, *Journal of High Energy Astrophysics*, 7, 148
- Komossa, S., & Bade, N. 1999, *A&A*, 343, 775
- Komossa, S., Halpern, J., Schartel, N., et al. 2004, *ApJL*, 603, L17
- Komossa, S., Zhou, H., Wang, T., et al. 2008, *ApJL*, 678, L13
- Kormendy, J., & Ho, L. C. 2013, *ARA&A*, 51, 511
- Kuin, N. P. M., Wu, K., Oates, S., et al. 2019, *MNRAS*, 487, 2505
- Law-Smith, J., Guillochon, J., & Ramirez-Ruiz, E. 2019, *ApJL*, 882, L25
- Law-Smith, J., Ramirez-Ruiz, E., Ellison, S. L., & Foley, R. J. 2017, *ApJ*, 850, 22
- Leloudas, G., Dai, L., Arcavi, I., et al. 2019, arXiv e-prints, arXiv:1903.03120
- Li, S., Liu, F. K., Berczik, P., & Spurzem, R. 2017, *ApJ*, 834, 195
- Li, L.-X., Narayan, R., & Menou, K. 2002, *ApJ*, 576, 753
- Lin, D., Godet, O., Ho, L. C., et al. 2017a, *MNRAS*, 468, 783
- Lin, D., Guillochon, J., Komossa, S., et al. 2017b, *Nature Astronomy*, 1, 0033
- Liu, F. K., & Chen, X. 2013, *ApJ*, 767, 18
- Liu, F. K., Li, S., & Chen, X. 2009, *ApJL*, 706, is L133
- Liu, F. K., Li, S., & Komossa, S. 2014, *ApJ*, 786, 103

- Liu, F. K., Zhou, Z. Q., Cao, R., Ho, L. C., & Komossa, S. 2017, *MNRAS*, 472, L99
- Lodato, G., King, A. R., & Pringle, J. E. 2009, *MNRAS*, 392, 332
- Lodato, G., & Rossi, E. 2011, *MNRAS*, 410, 359
- Lu, W., & Kumar, P. 2018, *ApJ*, 865, 128
- Magorrian, J., & Tremaine, S. 1999, *MNRAS*, 309, 447
- Magorrian, J., Tremaine, S., Richstone, D., et al. 1998, *AJ*, 115, 2285
- Maksym, W. P., Ulmer, M. P., & Eracleous, M. 2010, *ApJ*, 722, 1035
- Margutti, R., Metzger, B. D., Chornock, R., et al. 2019, *ApJ*, 872, 18
- McConnell, N. J., & Ma, C.-P. 2013, *ApJ*, 764, 184
- McKinney, W. 2010, in *Proceedings of the 9th Python in Science Conference*, ed. S. van der Walt & J. Millman, 51 – 56
- Miller, J. M., Kaastra, J. S., Miller, M. C., et al. 2015, *Nature*, 526, 542
- Mockler, B., Guillochon, J., & Ramirez-Ruiz, E. 2019, *ApJ*, 872, 151
- Newville, M., Stensitzki, T., Allen, D. B., & Ingargiola, A. 2014, *LMFIT: Non-Linear Least-Square Minimization and Curve-Fitting for Python, 0.8.0*, Zenodo
- Nicholl, M., Blanchard, P. K., Berger, E., et al. 2019, *MNRAS*, 488, 1878
- Onori, F., Cannizzaro, G., Jonker, P. G., et al. 2019, *MNRAS*, 489, 1463
- Paczynski, B. 1980, *AcA*, 30, 347
- Palaversa, L., Gezari, S., Sesar, B., et al. 2016, *ApJ*, 819, 151
- Perley, D. A., Mazzali, P. A., Yan, L., et al. 2019, *MNRAS*, 484, 1031
- Piran, T., Svirski, G., Krolik, J., Cheng, R. M., & Shiokawa, H. 2015, *ApJ*, 806, 164
- Popović, L. Č., Mediavilla, E., Bon, E., & Ilić, D. 2004, *A&A*, 423, 909
- Rees, M. J. 1988, *Nature*, 333, 523
- Reines, A. E., & Volonteri, M. 2015, *ApJ*, 813, 82
- Roth, N., Kasen, D., Guillochon, J., & Ramirez-Ruiz, E. 2016, *ApJ*, 827, 3
- Ryu, T., Krolik, J., Piran, T., & Noble, S. 2019, arXiv e-prints, arXiv:1907.11883
- Sądowski, A., Tejeda, E., Gafton, E., Rosswog, S., & Abarca, D. 2016, *MNRAS*, 458, 4250
- Saxton, C. J., Perets, H. B., & Baskin, A. 2018, *MNRAS*, 474, 3307
- Saxton, R. D., Read, A. M., Komossa, S., et al. 2017, *A&A*, 598, A29
- Saxton, R. D., Read, A. M., Komossa, S., et al. 2019, arXiv e-prints, arXiv:1908.01065
- She, R., Ho, L. C., & Feng, H. 2017, *ApJ*, 835, 223
- Shiokawa, H., Krolik, J. H., Cheng, R. M., Piran, T., & Noble, S. C. 2015, *ApJ*, 804, 85
- Stone, N. C., Generozov, A., Vasiliev, E., & Metzger, B. D. 2018, *MNRAS*, 480, 5060
- Stone, N. C., & Metzger, B. D. 2016, *MNRAS*, 455, 859
- Storchi-Bergmann, T., Baldwin, J. A., & Wilson, A. S. 1993, *ApJL*, 410, L11
- Storchi-Bergmann, T., Schimoia, J. S., Peterson, B. M., et al. 2017, *ApJ*, 835, 236
- Strateva, I. V., Strauss, M. A., Hao, L., et al. 2003, *AJ*, 126, 1720
- Strubbe, L. E., & Quataert, E. 2009, *MNRAS*, 400, 2070
- Svirski, G., Piran, T., & Krolik, J. 2017, *MNRAS*, 467, 1426
- Tejeda, E., & Rosswog, S. 2013, *MNRAS*, 433, 1930
- van den Bosch, R. C. E. 2016, *ApJ*, 831, 134
- van der Walt, S., Colbert, S. C., & Varoquaux, G. 2011, *Computing in Science and Engineering*, 13, 22
- van Velzen, S. 2018, *ApJ*, 852, 72
- van Velzen, S., Farrar, G. R., Gezari, S., et al. 2011, *ApJ*, 741, 73
- van Velzen, S., Gezari, S., Cenko, S. B., et al. 2019a, *ApJ*, 872, 198
- van Velzen, S., Stone, N. C., Metzger, B. D., et al. 2019b, *ApJ*, 878, 82
- Vinkó, J., Yuan, F., Quimby, R. M., et al. 2015, *ApJ*, 798, 12
- Wang, J., & Merritt, D. 2004, *ApJ*, 600, 149
- Wang, T.-G., Zhou, H.-Y., Komossa, S., et al. 2012, *ApJ*, 749, 115
- Wevers, T., Pasham, D. R., van Velzen, S., et al. 2019a, *MNRAS*, 488, 4816
- Wevers, T., Stone, N. C., van Velzen, S., et al. 2019b, *MNRAS*, 487, 4136
- Wevers, T., van Velzen, S., Jonker, P. G., et al. 2017, *MNRAS*, 471, 1694